INL/EXT-19-54502
Revision 0

Measurement of Kernel Swelling and Buffer Densification in Irradiated UCO and UO_2 TRISO Fuel Particles from AGR-2

John D. Stempien
Mitchell A. Plummer
Jason L. Schulthess

June 2019

The INL is a U.S. Department of Energy National Laboratory
operated by Battelle Energy Alliance

INL/EXT-19-54502
Revision 0

Measurement of Kernel Swelling and Buffer Densification in Irradiated UCO and UO2 TRISO Fuel Particles from AGR-2

John D. Stempien
Mitchell A. Plummer
Jason L. Schulthess

June 2019

Idaho National Laboratory
Idaho Falls, Idaho 83415

http://www.inl.gov

Prepared for the
U.S. Department of Energy
Office of Nuclear Energy
Under DOE Idaho Operations Office
Contract DE-AC07-05ID14517

Measurement of Kernel Swelling and Buffer Densification in Irradiated UCO and UO_2 TRISO Fuel Particles from AGR-2

INL/EXT-19-54502
Revision 0

June 2019

Approved by:

John D Stempien

John D. Stempien
AGR TRISO Fuel PIE Technical Lead

6/28/2019
Date

for

Paul A. Demkowicz
AGR Program Technical Director

6/28/2019
Date

Travis R. Mitchell
ART Program Manager

6/28/2019
Date

for

Michelle T. Sharp
INL Quality Engineer

6/28/2019
Date

SUMMARY

The second Advanced Gas Reactor irradiation (AGR-2) featured UCO tristructural isotropic (TRISO)-coated particle fuel and, for comparison purposes, UO_2 TRISO fuel. Particles from three UCO fuel compacts and one UO_2 fuel compact were chosen for analysis of kernel swelling and buffer densification (also called buffer shrinkage). Both kernel swelling and buffer shrinkage are common elements of TRISO fuel performance models. More recently, the AGR program has determined that buffer shrinkage may impact the integrity of the inner pyrolytic carbon (IPyC) layer, which may impact SiC layer integrity (particularly during high-temperature heating tests). Therefore, measurements of buffer irradiation-induced shrinkage may be useful in improving existing models and developing new models that capture buffer-IPyC-SiC-fission product interactions observed in recent AGR post-irradiation examination.

TRISO particles were mounted in epoxy, ground, polished, and imaged via optical microscopy in four separate iterations. Each of the four iterations revealed progressively deeper cross sections within the particles. Images collected from each iteration were analyzed for the circumferences/radii of the kernel, buffer, IPyC, and SiC. Spheres were fit to each set of measurements to generate spherical radii representative of the components of the fuel particle. From these radii, volumes were computed and compared to the as-fabricated volumes.

UCO kernel swelling was similar among the three AGR-2 compacts ranging from approximately 28 ± 7% to 32 ± 9%. This is only slightly higher swelling than was measured in an earlier study of an AGR-1 compact. However, the burnup at which this swelling occurred in AGR-2 was lower than in AGR-1, indicating a faster swelling rate for the AGR-2 kernels over the irradiation conditions covered by these compacts. The average AGR-2 UO_2 kernel swelling was less, at 10 ± 10%, a mean value comparable to other studies of UO_2 kernel swelling.

While AGR-2 UCO and UO_2 kernels demonstrated different rates of swelling, the extent of buffer shrinkage was similar among the two fuel types, ranging from 24 ± 26% to 28 ±20%. This is significantly less shrinkage than was observed for AGR-1 buffers. A commonly-observed post-irradiation particle morphology is one where the buffer pulls away from the IPyC (at least in some regions of the particle). Besides the possibility of the buffer degrading the IPyC when it pulls away, this gap is significant because it may also reduce heat transfer within the particle or alter transport of fission products from the buffer to the IPyC. Average AGR-2 buffer-IPyC gaps were similar for the UCO and UO_2 particles, ranging from 22 ± 6 μm to 26 ± 4 μm. This is similar to what was measured for AGR-1 Compact 1-3-1.

ACKNOWLEDGEMENTS

Critical contributions to this work were made by a number of people. Particles for this work were shipped from Oak Ridge National Laboratory (where Dr. John Hunn was the primary point of contact) to INL. Brian Frickey performed the materiolographic mounting (including mount design), grinding, and polishing at INL. Cassie Anderson-Thueson assisted in the materiolographic work. John Stanek and Francine Rice assisted in trials to improve and test the new mount design.

CONTENTS

SUMMARY vi

ACRONYMS xiii

1. INTRODUCTION 1
   - 1.1 Program Purpose 1
   - 1.2 Current Status of AGR Program Irradiations 1
   - 1.3 AGR-1 Fuel Description 2
   - 1.4 AGR-2 Fuel Description 3

2. AGR-2 PARTICLE CERAMOGRAPHY 4
   - 2.1 Purpose of Ceramography 4
   - 2.2 Basic Process Description 5
     - 2.2.1 Compact selection 6
     - 2.2.2 Particle processing and selection for mounting 6
     - 2.2.3 Particle mounting 7
     - 2.2.4 Grinding, backpotting, and polishing 10
     - 2.2.5 Microscopy and image acquisition 11
     - 2.2.6 Micrograph image processing 12

3. CALCULATIONS 15
   - 3.1 Mathematical Model 16
   - 3.2 Maximum Likelihood Fitting and Constraints 17
   - 3.3 Calculation of Changes in Radius and Volume 18
     - 3.3.1 Statistics of ratios of measurements 18
     - 3.3.2 Calculations of sphere and shell volumes 19
   - 3.4 Sources of Uncertainty 19
     - 3.4.1 Tracing interfaces versus best-fit circle 19
     - 3.4.2 Effects of layer interface roughness and irregularities 20
     - 3.4.3 Effects of subjectivity and repeatability 23

4. RESULTS 23
   - 4.1 TRISO Particle Radii 23
   - 4.2 Kernel Swelling and Buffer Shrinkage 30
   - 4.3 Post-irradiation Buffer-IPyC gap 33
   - 4.4 Comparison to prior measurements 34

5. CONCLUSIONS 37

6. REFERENCES 37

FIGURES

Figure 1. TAVA irradiation temperatures versus burnup for compacts from the AGR-1 and AGR-2 irradiations. AGR-1 burnups and temperatures from (Sterbentz 2013) and (Hawkes 2014a), respectively. AGR-2 burnups and temperatures from (Sterbentz 2014) and (Hawkes 2014b), respectively. 2

Figure 2. X-radiographs of U.S. UCO (compact LEU09-OP2-Z002, left) and UO_2 (compact LEU11-OP2-Z018, right) compacts taken from the same compact lots used in the AGR-2 irradiation. Note the visibly lower packing fraction of the UO_2 compact. Images from (Hunn et al. 2010). 4

Figure 3. Simplified ceramography process flow diagram. 5

Figure 4. Four different cross sections taken at four different levels within AGR-2 particle 3-3 from Mount 26B from Compact 5-4-2. Top left: cross section 1 (shallowest depth in particle). Top right: cross section two. Bottom left: cross section 3. Bottom right: cross section 4 (just above particle mid-plane). 6

Figure 5. Rendering (silver images) of mount designed for AGR-2 ceramography and pictures (brown images) of fabricated Micarta mount. 8

Figure 6. Pouring particles from the vial into the mount. Two funnels were used to ease pouring process. 9

Figure 7. Mount with particles in the wells, adhered to Wafermount at the bottom of the wells, prior to addition of epoxy. 9

Figure 8. Montage of multiple 5X magnification micrographs taken of MNT88A. Examples of gas bubbles trapped in the epoxy are highlighted. 10

Figure 9. “Containment box” at HFEF Window 2M. 11

Figure 10. Microscopes available in the “Met Box” at HFEF. The Leica microscope was used for AGR-2 ceramography 12

Figure 11. Backlit silhouette of Mount 86A, Cross Section 1, Particle 2-8, from Compact 6-3-3. 13

Figure 12. Images and original measurements of AGR-1 particle 002 from Compact 1-3-1, Mount 31V. The white outlines are the circles fitted to 15 user-selected points around the inner or outer boundary of the kernel or layer. 14

Figure 13. Images, new measurements, and % difference between the old and new measurements of AGR-1 particle 002 from Compact 1-3-1, Mount 31V. 14

Figure 14. Compact 5-4-2 Particle 1-2, Cross section 3 from Mount 30B, showing extrusion of the kernel through the fractured region of the buffer layer. Particles such as this were excluded from quantitative analysis of the buffer and kernel. 15

Figure 15. Geometry of an idealized particle. Compare with a typical particle in Figure 17. 17

Figure 16. Ratio of best-fit circle radius to the radius calculated from the circumference (perimeter) of an ellipse versus the eccentricity of the ellipse 20

Figure 17. The second cross section of Particle 12-1 in Mount 86A from Compact 6-3-3. Boundary tracings are shown in red. Eccentricity of the kernel trace is 0.44, for which the ratio of lengths of the minor and major axes is 0.9. 20

Figure 18. Illustration of periodic irregularities in a circular trace that would produce a +5% error (A) and a +10% error (B) in the radius calculated from measured circumference. Yellow curves reflect 100 points evenly distributed along, and to either side of the true circumference. Red curves denote actual traces used in the analysis of this particle (C)........... 21

Figure 19. Mount 82A, Cross section 4, Particle 12-4 from UO_2 Compact 3-3-1 (particle ID: MNT82A-CS4-12-4). Red arrows show strips of buffer bridging the IPyC-buffer gap. Blue arrow shows significant buffer fragment adhered to IPyC. 22

Figure 20. Optical micrograph of Mount 86A, Cross section 4, Particle 5-5 (from UCO Compact 6-3-3). Enlarged region shows example of a uranium carbide skin surrounding the kernel. 23

Figure 21. Histograms for radii for particles from AGR-2 UO_2 Compact 3-3-1. PIE distribution parameters (i.e., SD) are for the distribution of fitted means. The SD for the distribution, incorporating the uncertainty of the fit, is given parenthetically............................ 25

Figure 22. Histograms of radii for particles from AGR-2 UCO Compact 6-3-3. PIE distribution parameters (i.e., SD) are for the distribution of fitted means. The SD for the distribution, incorporating the uncertainty of the fit, is given parenthetically............................ 26

Figure 23. Histograms of radii for particles from AGR-2 UCO Compact 5-4-2. PIE distribution parameters (i.e., SD) are for the distribution of fitted means. The SD for the distribution, incorporating the uncertainty of the fit, is given parenthetically............................ 27

Figure 24. Histograms of radii for particles from AGR-2 UCO Compact 5-3-3. PIE distribution parameters (i.e., SD) are for the distribution of fitted means. The SD for the distribution, incorporating the uncertainty of the fit, is given parenthetically............................ 28

Figure 25. Histograms of radii from combining the data from all AGR-2 UCO compacts analyzed in this study. PIE distribution parameters (i.e., SD) are for the distribution of fitted means. The SD for the distribution, incorporating the uncertainty of the fit, is given parenthetically. 29

Figure 26. Histograms of kernel and buffer volumetric changes in each AGR-2 compact. The bottom-most histograms combine the values from the three UCO compacts (i.e., 6-3-3, 5-4-2, and 5-3-3) into a single population. PIE distribution parameters are for the distribution of fitted means. 31

Figure 27. Ratio of PIE kernel volume to as-fabricated volume versus compact burnup. AGR-1 Compact 1-3-1 is also included. Mean and variance of the ratio were calculated as described in Section 3.3.1, with variance of the PIE groups estimated from the distribution of fitted values. 32

Figure 28. Ratio of PIE buffer volume to as-fabricated volume versus fast neutron fluence (E>0.18MeV). AGR-1 Compact 1-3-1 is also included. 33

Figure 29. Size of the gap between the buffer and IPyC layers as a function of fast neutron fluence (E>0.18MeV). 34

Figure 30. Kernel volume ratio (irradiated/as-fabricated) for UCO, UO_2, and UC_2 coated particles.. 35

TABLES

Table 1. General AGR-1 Capsule 1 fuel properties and irradiation parameters specific to AGR-1 Compact 1-3-1. Fuel fabrication properties and irradiation parameters from (Collin 2015a). 3

Table 2. Summary of selected AGR-2 UCO and UO_2 TRISO particle properties and compact properties. 4

Table 3. Compact properties and particle mount identifiers. 7

Table 4. As-fabricated fuel kernel data, irradiation conditions, and kernel volume change data for UCO, UO_2, and UC_2 coated particles. 36

ACRONYMS

AGR	Advanced Gas Reactor.
ANOVA	analysis of variance
ART	Advanced Reactor Technologies
ATR	Advanced Test Reactor
BISO	bistructural isotropic
FIMA	fissions per initial heavy metal atom
HFEF	Hot Fuel Examination Facility
HTGR	high temperature gas-cooled reactor
INL	Idaho National Laboratory
IPyC	inner pyrolytic carbon
LAS	Leica Application Suite
LBL	leach-burn-leach
MLE	maximum likelihood estimate
NA	not available
N/A	not applicable
OPyC	outer pyrolytic carbon
ORNL	Oak Ridge National Laboratory
PIE	post-irradiation examination
SD	standard deviation
SiC	silicon carbide
TAVA	time-averaged volume-averaged
TRISO	tristructural isotropic
UCO	uranium oxycarbide
UO_2	uranium dioxide

Measurement of Kernel Swelling and Buffer Densification in Irradiated UCO and UO_2 TRISO Fuel Particles from AGR-2

1. INTRODUCTION

1.1 Program Purpose

The Advanced Gas Reactor (AGR) Fuel Development and Qualification Program was established to perform research and development on tristructural isotropic (TRISO)-coated particle fuel to support deployment of a high-temperature gas-cooled reactor (HTGR). This work continues as part of the Advanced Reactor Technologies (ART) TRISO Fuel Program. The overarching goal of the ART AGR program is to provide a baseline fuel qualification data set to support licensing and operation of an HTGR. To achieve these goals, the program includes the elements of fuel fabrication, irradiation, post-irradiation examination (PIE) and safety/heating testing, fuel performance modeling, and fission product transport (INL 2018). Several fuel irradiation experiments have been performed at the Advanced Test Reactor (ATR) at Idaho National Laboratory (INL), and a fourth irradiation began in February 2018. These experiments are intended to provide data on fuel performance under irradiation, support fuel fabrication process development, qualify fuel for operating and accident conditions, provide irradiated fuel for accident testing, and support development of fuel performance and fission product transport models.

1.2 Current Status of AGR Program Irradiations

The first two AGR fuel irradiation experiments (AGR-1 and AGR-2) had similar test train designs, and one of the objectives was to test TRISO-coated particle fuel performance over a range of irradiation temperatures and burnups. AGR fuel kernels are a heterogeneous mixture of uranium carbide and uranium oxide (UCO). Figure 1 shows the time-averaged, volume-averaged (TAVA) irradiation temperature and burnup for each AGR-1 and AGR-2 fuel compact. Burnup is given as percent fissions per initial metal atom (FIMA). AGR-2 TRISO coatings were fabricated using conditions derived from the AGR-1 Variant 3 fuel, and while the AGR-1 coatings were produced at the lab-scale, AGR-2 coatings were produced in a 6-in diameter, engineering scale coater (Demkowicz 2013, INL 2018).

In addition to AGR UCO fuel (in Capsules 2, 5, and 6), the AGR-2 experiment also had UO_2 fuel (in Capsule 3) to compare the performance of UCO versus UO_2 and to compare to UO_2 fuel performance observed historically in the German TRISO fuel program.[a] AGR-1 was irradiated in the B-10 position in ATR from December 2006 to November 2009 (Collin 2015a). AGR-2 was irradiated in the B-12 position of ATR from June 2010 to October 2013 (Collin 2018a). The major elements of AGR-1 PIE are complete (Demkowicz et al. 2015, Demkowicz et al. 2016). AGR-2 PIE began in July 2014, is still in-progress, and encompasses as-irradiated analyses, reirradiations, heating testing, microscopy, and other activities.

The third irradiation experiment, AGR-3/4, was designed to investigate the migration of fission products in fuel compact graphitic matrix and reactor graphite components. AGR-3/4 was irradiated in the northeast flux trap of ATR, from December 2011 to April 2014 (Collin 2015b). The experiment consisted of fuel compacts containing TRISO-coated driver-fuel particles similar to AGR-1 baseline fuel (Collin 2015b) and designed-to-fail particles that are designed to release fission products during irradiation, which will migrate through the surrounding cylindrical rings of graphitic matrix and nuclear-grade graphite. AGR-3/4 PIE is in progress and will provide data to support refinement of fission

---

[a] The AGR-2 irradiation had 6 irradiation capsules. Capsules 2, 3, 5, and 6 were US AGR capsules. Capsules 1 and 4 were French and South African fuel, respectively (Collin 2018a). Capsule 1 and 4 fuel compacts are not shown in Figure 1.

product transport models and HTGR source-term analyses (Demkowicz 2017). The fourth irradiation experiment, AGR-5/6/7 (Collin 2018b), started in ATR in February 2018 and serves as the fuel qualification irradiation.

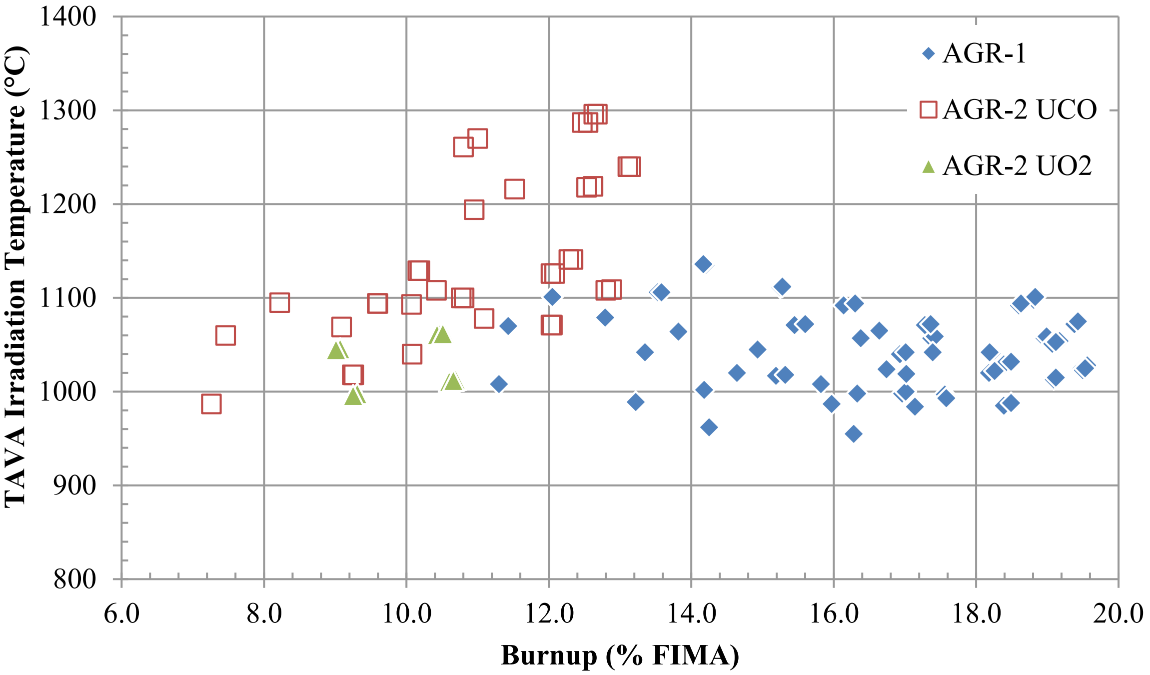

Figure 1. TAVA irradiation temperatures versus burnup for compacts from the AGR-1 and AGR-2 irradiations. AGR-1 burnups and temperatures from (Sterbentz 2013) and (Hawkes 2014a), respectively. AGR-2 burnups and temperatures from (Sterbentz 2014) and (Hawkes 2014b), respectively.

1.3 AGR-1 Fuel Description

AGR-2 fuel is the subject of the present study and experimental work; however, comparisons to the same type of work performed previously on particles from AGR-1 Compact 1-3-1 (Bower et al. 2017) will be made in subsequent sections. To aid in this comparison, Table 1 summarizes major irradiation parameters and properties of AGR-1 Compact 1-3-1. AGR-1 fuel particles had 350-µm-diameter UCO fuel kernels fabricated at BWXT in Lynchburg, Virginia. The enrichment was 19.7 weight % U-235. The kernels were TRISO-coated, overcoated in a precursor to graphitic matrix, and pressed into cylindrical compacts (nominally 25 mm long and 12.4 mm in diameter) at Oak Ridge National Laboratory (ORNL).

Table 1. General AGR-1 Capsule 1 fuel properties and irradiation parameters specific to AGR-1 Compact 1-3-1. Fuel fabrication properties and irradiation parameters from (Collin 2015a).

Fabrication Properties for AGR-1 Capsule 1 Compacts	
U-235 enrichment (wt %)	19.736
Kernel diameter (μm)	349.7
Buffer thickness (μm)	104.2
IPyC thickness (μm)	38.8
SiC thickness (μm)	35.9
OPyC thickness (μm)	39.3
Overall particle diameter (μm)	795.1
Number of particles per compact	4126
Particle volume packing fraction (%)	36.04
Irradiation Parameters Specific to AGR-1 Compact 1-3-1	
Compact Burnup (% FIMA)	16.14
Compact Fast Fluence (10^{25} n/m^2, E > 0.18 MeV)	3.22
TAVA Irradiation Temperature (°C)	1092

1.4 AGR-2 Fuel Description

AGR-2 Capsules 2, 3, 5, and 6 contained U.S. AGR program fuel. Capsules 1 and 4 contained French and South African fuel, respectively. Capsules 1 and 4 will not be discussed in this report. AGR-2 Capsules 2, 5, and 6 contained only U.S. UCO fuel, and Capsule 3 contained only U.S. UO_2 fuel. The kernels and the TRISO-coated particles were fabricated at BWXT, and the compacts were fabricated at ORNL. The UCO kernels were approximately 425 μm in diameter and were enriched to 14.0 weight % U-235. The UO_2 kernels were fabricated to dimensions and enrichments comparable to the German and South African pebble-bed HTGR fuel designs. UO_2 kernels were approximately 500 μm in diameter and were enriched to 9.60 weight % U-235. Once the TRISO coatings had been applied to the kernels, the particles were overcoated and compacted into cylinders, nominally 25.1 mm long and 12.3 mm in diameter, at ORNL. UCO compacts had a volume packing fraction of 37%, and UO_2 compacts had a volume packing fraction of 23%. Figure 2 shows x-ray radiographs of a UCO compact (left) and a UO_2 compact (right). There were approximately 3176 TRISO-coated fuel particles in each UCO compact and 1543 fuel particles in each UO_2 compact. A summary of major TRISO particle and fuel compact properties is given in the *AGR-2 Irradiation Test Final As-Run Report* (Collin 2018a). Detailed characterization data of the as-fabricated kernels, particles, and compacts have been compiled in reports referenced in (Collin 2018a). Select fuel properties from tables in Appendix A of (Collin 2018a) are given below in Table 2. The specific AGR-2 compacts chosen for ceramography and their irradiation parameters are discussed in Section 2.2.1.

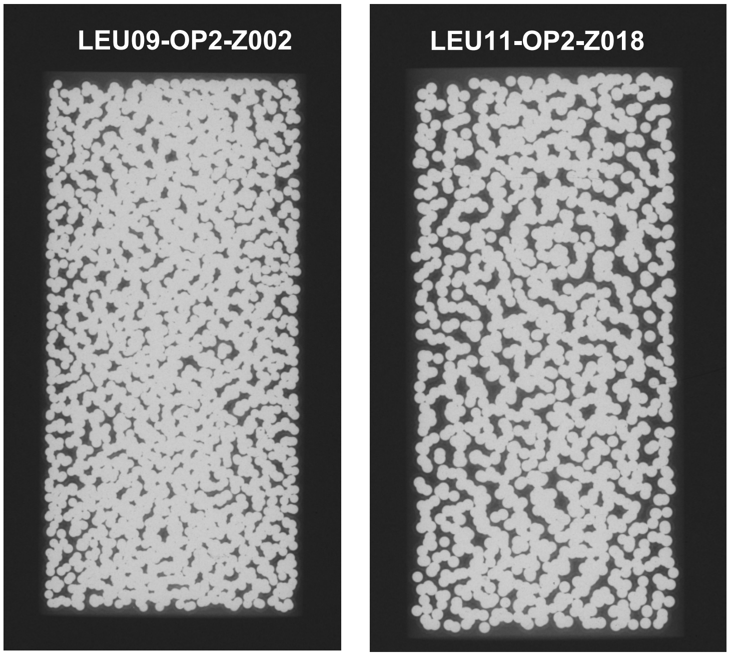

Figure 2. X-radiographs of U.S. UCO (compact LEU09-OP2-Z002, left) and UO_2 (compact LEU11-OP2-Z018, right) compacts taken from the same compact lots used in the AGR-2 irradiation. Note the visibly lower packing fraction of the UO_2 compact. Images from (Hunn et al. 2010).

Table 2. Summary of selected AGR-2 UCO and UO_2 TRISO particle properties and compact properties.

Property	Mean Value and Standard Deviation	
	UCO	UO_2
U-235 enrichment (wt %)	14.029 ± 0.026	9.600 ± 0.010
Kernel diameter (μm)	426.7 ± 8.8	507.7 ± 11.9
Buffer thickness (μm)	98.9 ± 8.4	97.7 ± 9.9
IPyC thickness (μm)	40.4 ± 2.5	41.9 ± 3.2
SiC thickness (μm)	35.2 ± 1.2	37.5 ± 1.2
OPyC thickness (μm)	43.4 ± 2.9	45.6 ± 2.4
Overall particle diameter (μm)	873.2 ± 23	953.0 ± 28
Number of particles per compact	3176	1543
Particle volume packing fraction	0.37	0.23

2. AGR-2 PARTICLE CERAMOGRAPHY

2.1 Purpose of Ceramography

The SiC layer is the primary structural layer of the TRISO system, and while intact pyrocarbon layers can provide hermeticity, retaining fission gases even when a defective SiC layer is present, the SiC layer is required for the TRISO particle to retain metallic fission products. Two phenomena included in TRISO fuel performance models such as the PARticle FUel ModEl (PARFUME) are kernel swelling and buffer densification (also referred to as buffer shrinkage) (Miller et al. 2018). PIE has shown that behavior of the buffer and inner pyrolytic carbon (IPyC) layer has an impact on the integrity of the SiC layer. SiC layer failure in irradiated AGR-1 and AGR-2 UCO particles was infrequent (Demkowicz et al. 2016, Hunn et al. 2018); however, when a particle with a failed SiC layer was found, the same mechanism was commonly observed (Hunn et al. 2016). With a sufficiently strong buffer-IPyC bond strength, shrinkage of the buffer can pull on the IPyC layer. This occurs because irradiation-induced buffer shrinkage exceeds any shrinkage of the IPyC layer, and the IPyC layer is generally well-bonded to the SiC layer. This can cause a fracture in the IPyC, and this IPyC fracture can then allow fission products (particularly Pd) to concentrate at the SiC layer inner surface. PIE has shown that Pd can form Pd-silicides in the SiC layer, leaving carbon-rich zones within the SiC layer (Gerczak et al. 2018, van Rooyen et al. 2014). These carbon rich zones are effectively perforations in the SiC layer and allow migration of metallic fission products (e.g., cesium) beyond the SiC layer. This study focuses on kernel swelling and buffer densification, two phenomena important for determining the buffer-IPyC gap size, and potentially of importance to develop models that will predict buffer-IPyC separation behavior.

2.2 Basic Process Description

The goal was to measure the kernel circumference and circumferences of the TRISO layers in a number of UCO and UO_2 particles at multiple levels within the particles using a series of grinding, polishing, imaging, and image processing steps. Figure 3 shows a basic flow diagram of the processes. Each process will be described in greater detail in the following subsections. Figure 4 shows four cross sections obtained at four levels above the mid-plane of AGR-2 UCO Compact 5-4-2 (Particle 3-3 from Mount 26B). A mathematical model is used to fit a sphere to the measurements obtained from image processing in order to determine the extent of kernel swelling and buffer densification in each particle. The layer and kernel morphology were also noted at each level.

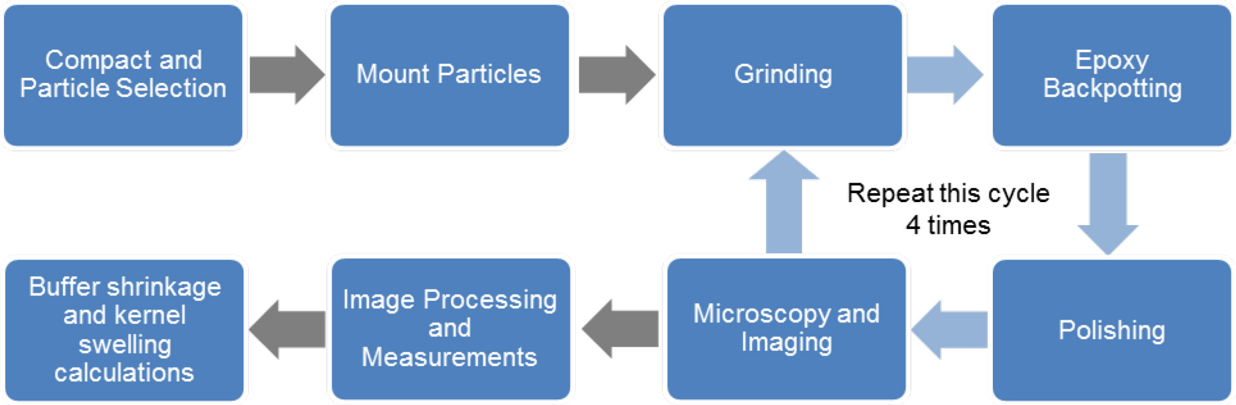

Figure 3. Simplified ceramography process flow diagram.

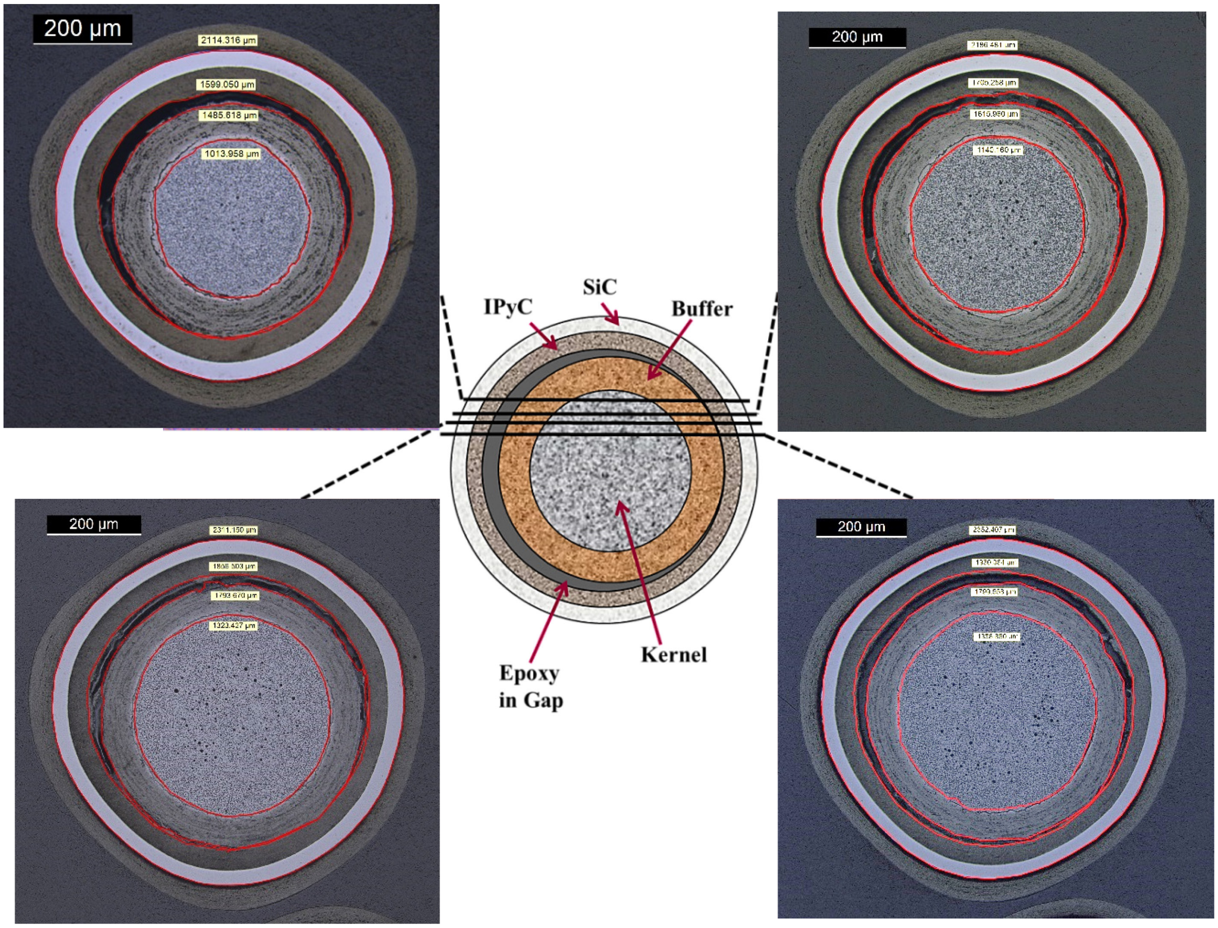

Figure 4. Four different cross sections taken at four different levels within AGR-2 particle 3-3 from Mount 26B from Compact 5-4-2. Top left: cross section 1 (shallowest depth in particle). Top right: cross section two. Bottom left: cross section 3. Bottom right: cross section 4 (just above particle mid-plane).

2.2.1 Compact selection

Three AGR-2 UCO compacts were chosen spanning burnups from 7.5 to 12.0 % FIMA and TAVA irradiation temperatures from 1060-1093°C. One AGR-2 UO_2 compact with a burnup and irradiation temperature that fit within the burnup and temperature ranges for the UCO compacts was also analyzed. Table 3 lists the chosen compacts, selected irradiation properties for each compact, vial numbers used to ship each group of particles from ORNL to INL, and the identifiers given to each ceramographic mount.

2.2.2 Particle processing and selection for mounting

Each of the four compacts was electrolytically deconsolidated at ORNL. Approximately 10% of the particles in each compact were separated from the rest of the particles prior to burn-leach analysis. The rest of the particles proceeded through the leach-burn-leach (LBL) process to measure the inventory of fission products outside of the SiC layer. For ceramography, particles from Compacts 3-3-1, 6-3-3, and 5-3-3 were riffled out of the group of particles that had completed the LBL process. Thus, particles from these three compacts had the OPyC layer removed, leaving the SiC layer as the outermost layer. The particles from Compact 5-4-2, however, had only undergone deconsolidation and pre-burn leaching, and therefore, had all TRISO layers intact. For each compact, particles were randomly selected and placed in several vials. Each vial had 100 particles. Two hundred particles (two vials worth) were used from each of Compacts 3-3-1 and 6-3-3. Prior compact ceramography (Rice et al. 2018) indicated a high-frequency of buffer fracture in compacts from Capsule 5. Particles with buffer fractures are not well-suited to buffer shrinkage and kernel swelling measurements; therefore, 300 particles were used from each of Compacts 5-4-2 and 5-3-3 with the expectation that many of these particles (with cracked buffer layers) would have to be excluded from analysis. In addition to other properties and identifiers, Table 3 also lists the number of particles in each mount with cross sections and measurements that were acceptable for measurements of kernel swelling and buffer shrinkage.

Table 3. Compact properties and particle mount identifiers.

Compact	Fuel Kernel Type	Compact Burnup (% FIMA)	Compact Fast Fluence (10^{25} n/m^2, E > 0.18 MeV)	TAVA Irradiation Temperature (°C)	Particle Vial Number	Mount ID	# of acceptable particles
3-3-1	UO_2	10.46	3.49	1062	1615	MNT82A	59
						MNT83A	33
					1616	MNT84A	58
						MNT85A	25
6-3-3	UCO	7.46	2.14	1060	1611	MNT86A	47
						MNT87A	15
					1612	MNT88A	29
						MNT89A	6
5-4-2	UCO	12.03	3.14	1071	1622	MNT26B	18
						MNT27B	10
					1623	MNT28B	21
						MNT29B	0
					1624	MNT30B	17
						MNT31B	10
5-3-3	UCO	10.07	2.91	1093	1610	MNT32B	19
						MNT33B	3
					168	MNT34B	17
						MNT35B	10
					169	MNT36B	17
						MNT37B	6
Totals	N/A	N/A	N/A	N/A	N/A	Total # Mounts: 20	Total # Acceptable Particles: 420

N/A: not applicable

2.2.3 Particle mounting

Each vial of 100 particles was used to make two mounts: one mount with approximately 80 particles, and a second mount with approximately 20 particles. Each mount was fabricated at INL from Micarta, and consisted of 12 individual wells and a central distributor to direct the individual particles to the wells when the particles were poured into the mount (see Figure 5). The mount was pressed over a semi-rigid, solvent-resistant plastic film with a pressure-sensitive, soluble adhesive (Wafermount-559). An aluminum funnel fabricated at INL was used to direct the particles into the wells (Figure 6). Once in the well, the particles were held in place at the bottom of the well by the adhesive film (Figure 7). Then a two-part epoxy (Buehler EPOHeat CLR) was poured into the mount to fix the particles in-place for grinding and polishing. As an example, Figure 8 shows particles in a mount after pouring the epoxy into the mount. Using a translucent epoxy enabled a measurement of the particle outer surface radius via a silhouette. Comparing the measured outer surface radius from each polished plane to the silhouette enables one to determine the depth of the cross sectioned surface within each particle.

Different mount designs and epoxies were experimented with using surrogate particles with the goal being to find a configuration that kept the particles at roughly the same level. If particles were at significantly different levels (distances from the surface) in the mount, it is possible that after one step of grinding, fuel kernels would be visible in only some of the particles in the mount. More grinding and polishing steps would be required to attain appropriate images of all particles. In a traditional mount with a single, large well, significant epoxy shrinkage occurred so that the particles were not at the same level. It was found that the effects of epoxy shrinkage were reduced with multiple, small wells.

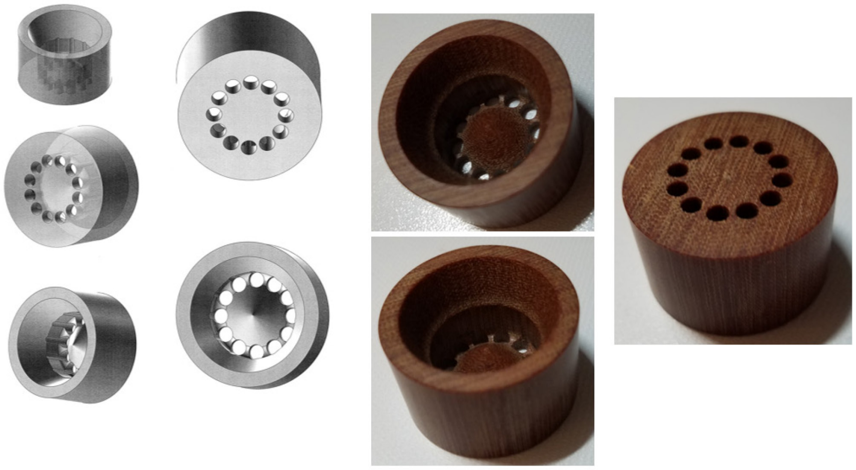

Figure 5. Rendering (silver images) of mount designed for AGR-2 ceramography and pictures (brown images) of fabricated Micarta mount.

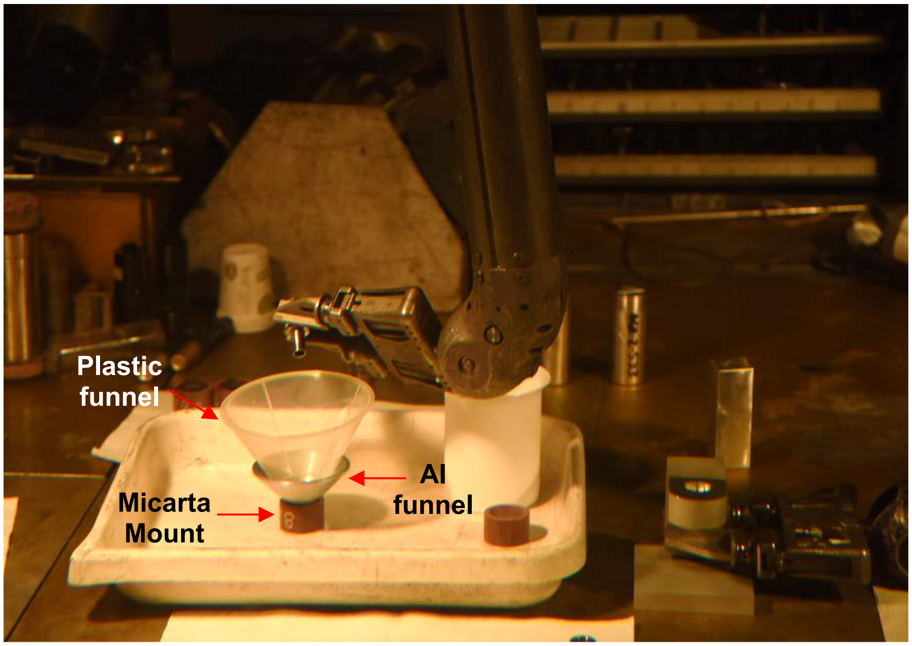

Figure 6. Pouring particles from the vial into the mount. Two funnels were used to ease pouring process.

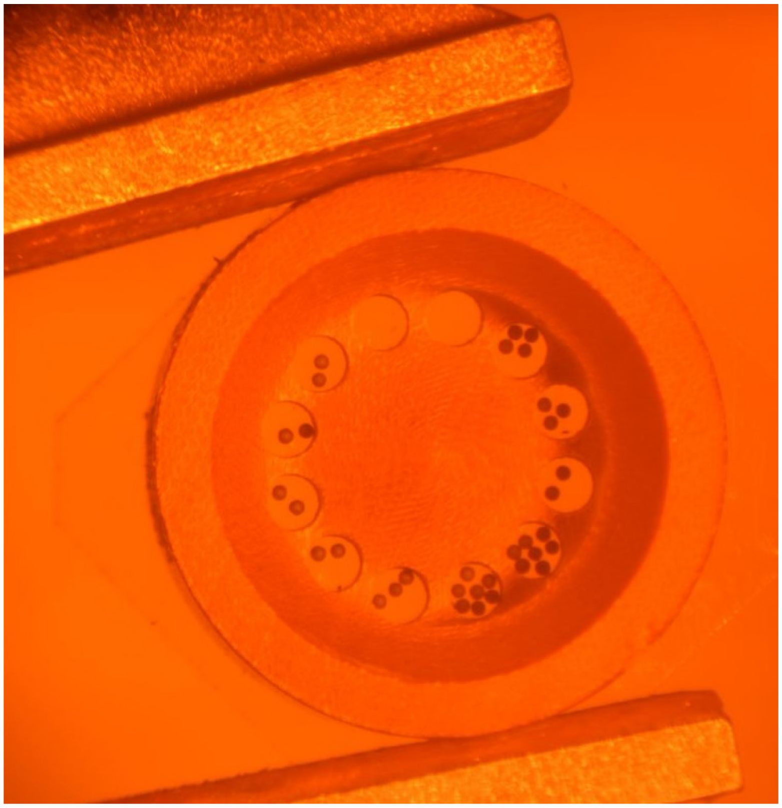

Figure 7. Mount with particles in the wells, adhered to Wafermount at the bottom of the wells, prior to addition of epoxy.

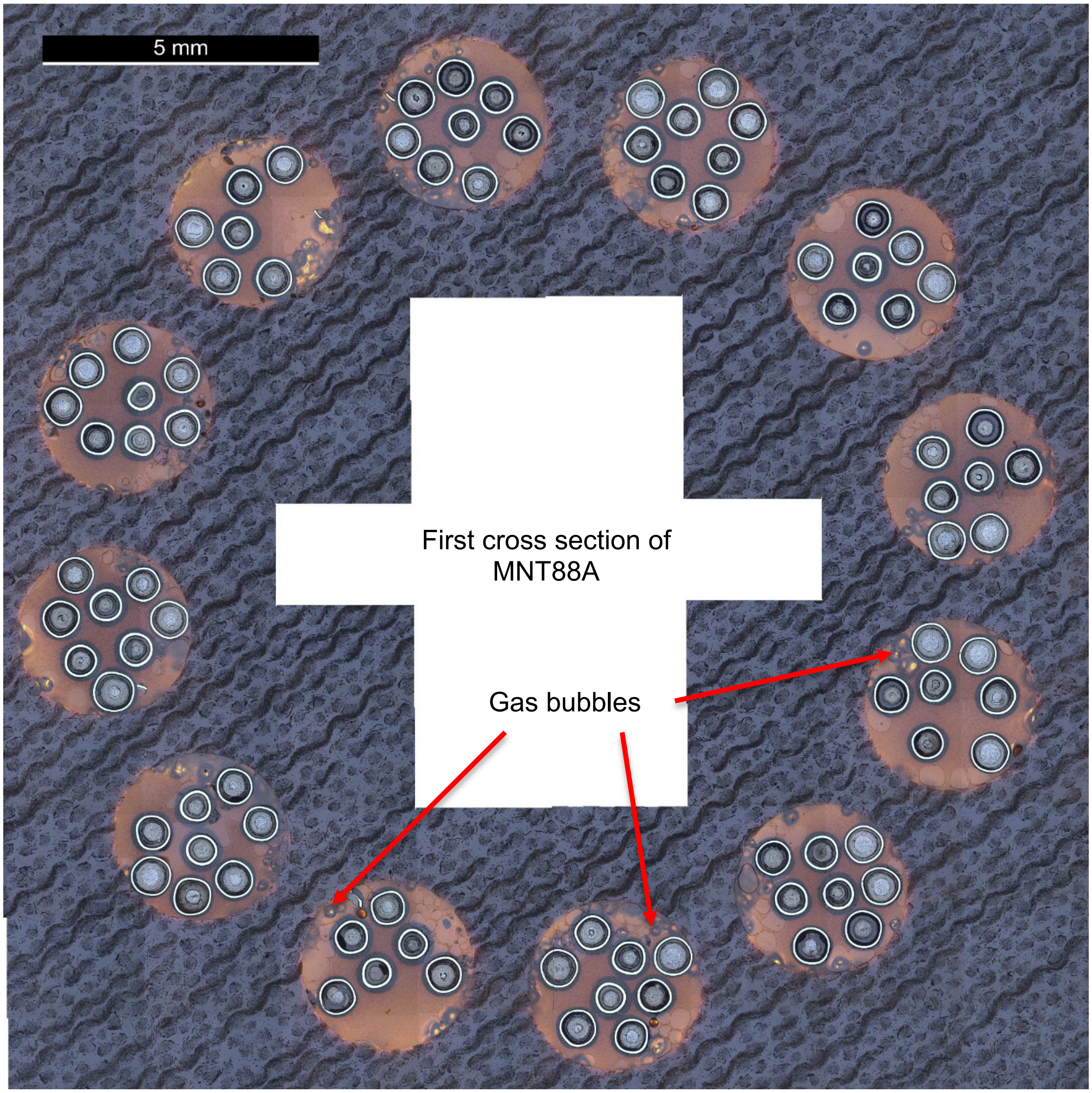

Figure 8. Montage of multiple 5X magnification micrographs taken of MNT88A. Examples of gas bubbles trapped in the epoxy are highlighted.

2.2.4 Grinding, backpotting, and polishing

The grinding, backpotting, and polishing steps occurred in the "Containment Box" at Window 2M at the Hot Fuels Examination Facility (HFEF). Figure 9 shows the polishing and grinding equipment used at Window 2M. (The low-speed saw was not used.) The grinding and polishing systems are Struers Tegrapol units that have been modified at INL to support remote operations within the HFEF hot cell.

After setting the particles with epoxy in the mount, a large meniscus formed on the upper surface of the mount as the epoxy cured. Initial attempts to grind the bottom mount surface (where the particles were located) resulted in uneven grinding. It was identified that the meniscus at the top of the mount resulted in non-axial force being applied to the mount, which caused the uneven grinding. This was resolved by first grinding the top surface (non-particle side) to create a flat surface followed by grinding of the bottom surface (particle side).

Grinding was performed using a 1200 grit grinding pad with ~20N of force during more aggressive grinding operations and as little as ~5N of force during less aggressive grinding operations. After each round of grinding, the mounts were inspected via the Containment Box periscope. Each mount was also dimensionally measured between grinding steps to quantify the amount of material removed from the mount. For approximately each 0.0762 mm (0.003 in) of material removed, the particles side of the mount was backpotted to fill voids made accessible via grinding, and then subjected to vacuum to aid with ingress of epoxy into the voids and remove gas bubbles. Frequent backpotting fixed the particles in place, supported the TRISO layers, and prevented loss of the fuel kernels during subsequent grinding operations.

Once an adequate amount of material was removed, exposing all of the layers on nearly all of the particles, polishing was performed using a Struers MD-Mol pad and a 3 μm diamond suspension followed by a Struers MD-Nap pad and a 1 μm diamond suspension. Prior to data/image acquisition, adequate polishing was confirmed via the Leica optical microscope in the "Met Box" at HFEF. As necessary, additional polishing was performed to ensure the quality of the surface preparation.

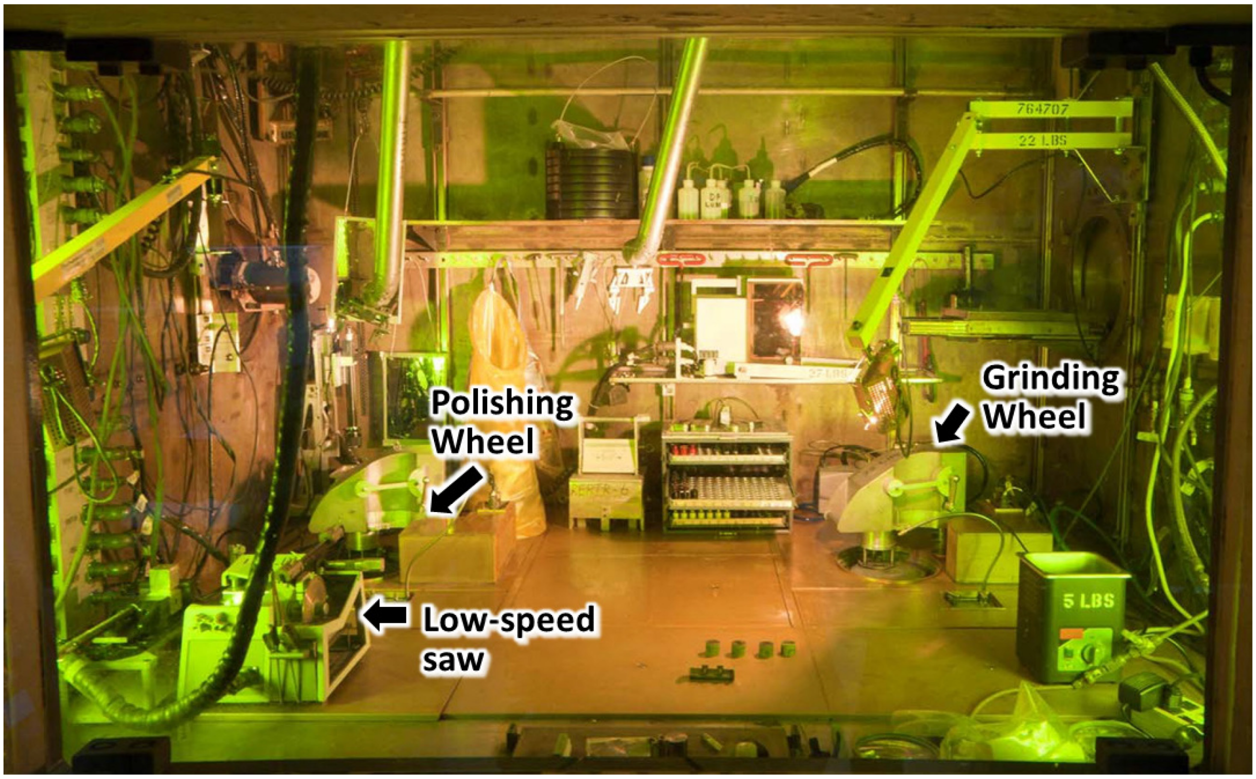

Figure 9. "Containment box" at HFEF Window 2M.

2.2.5 Microscopy and image acquisition

After polishing in the Containment Box, the mounts were transferred via a pneumatically-actuated capsule to the Met Box for imaging. A Leica optical microscope in the HFEF Met Box (see Figure 10) was used to acquire micrographs of the mount surfaces and each particle within the mount after each round of grinding, backpotting, and polishing. After imaging, the mounts were then transferred back to the Containment Box for additional grinding, backpotting, and polishing as-appropriate.

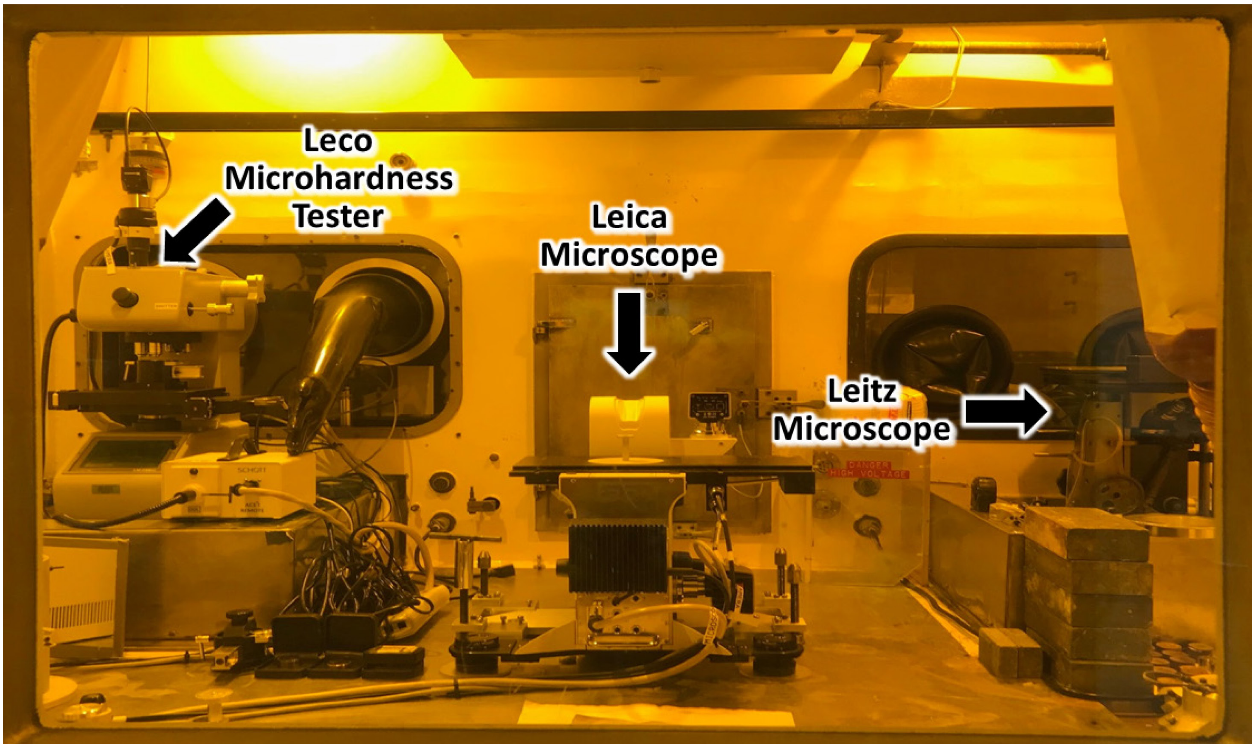

Figure 10. Microscopes available in the “Met Box” at HFEF. The Leica microscope was used for AGR-2 ceramography.

2.2.6 Micrograph image processing

2.2.6.1 Measurement method and comparison

A study of kernel swelling and buffer shrinkage was performed previously on AGR-1 fuel (Bower et al. 2017). AGR-1 ceramography measurements were performed using the Leitz Metallograph installed in the HFEF Met Box (see Figure 10), where images were captured of both individual particles and a calibration stage. The settings of the Leitz Metallograph were the same between the two images, allowing for quantitative measurements to be made using a pixel-to-micrometer relationship applied using the post-processing software, PAX-it. In contrast, AGR-2 data were collected on a recently-installed Leica optical microscope in the Met Box (see Figure 10). The Leica microscope is set up with a traceable standard to calibrate the pixel-to-micrometer relationship, allowing for quantitative dimensional measurements to be made directly using the Leica Application Suite software (LAS).

Two types of measurements were made. The first type of measurement was of the particle overall diameter. To obtain the full diameter of a particle at the outermost layer at the particle midplane (or equator), each particle in the translucent mounts was backlit using LED lights to provide a projected shadow (silhouette) that was observed through the microscope. Figure 11 shows an example of a particle silhouette. The microscope was then focused on the edge of the silhouette, which is why the surface of the particle is out-of-focus. The LAS software was then used to perform analysis of the diameter of the silhouette by using greyscale threshold to select the area of interest. The LAS software allowed the automation of this analysis after input of user-defined values such as the selected greyscale. It is estimated that this routine located the edge of the silhouette to within +/- 3 pixels such that the silhouette diameter was known to within +/- 0.3 μm.

Figure 11. Backlit silhouette of Mount 86A, Cross Section 1, Particle 2-8, from Compact 6-3-3.

The second set of measurements were made on the kernel perimeter, buffer outer perimeter, IPyC inner perimeter, and SiC outer perimeter from the images of the particle cross sections. In the AGR-1 study, post-processing of particle cross section images was done in PAX-it. Using PAX-it, a circle was fit to 16 user-selected points around the boundary of the kernel and/or a given layer to determine the kernel radius and the inner and outer radii of the layer. Figure 12 shows the original images of an AGR-1 particle, the circles (white outlines) fit to the 16 points manually placed on the boundary of each layer, and the resultant radii at different levels within the particle.

The same types of measurements were made on AGR-2 particle cross sections; however, the LAS software allowed for measurements of the perimeter to be made directly (without post-processing). Furthermore, rather than fitting a circle to 16 user-selected points, a new method was used that draws straight-line segments between 100 user-selected points to give a perimeter. The perimeter was assumed to be a circumference of the layer (i.e., the particle is assumed to be spherical and its cross section is assumed to be circular), and a radius was calculated from the circumference. A benefit of the new method is the ability to more accurately follow interfaces of layers that depart from sphericity.

To ensure that measurements made with the two methods are comparable, images of a particle and calibration stage from the work performed on AGR-1 were re-analyzed using the new microscope, software, and method. The original radii for the four different levels are shown in Figure 12. Figure 13 shows the original images of the same AGR-1 particle, the perimeter from the new method (red outlines) applied to each layer by selecting 100 points around the feature, the resultant radii calculated from the perimeters, and a comparison to the radii determined from the original method. The results show that the radii determined by measurements between the two systems are generally within ~3-5 μm (typically < 3%), indicating reasonable agreement between the two methods for this particular particle.

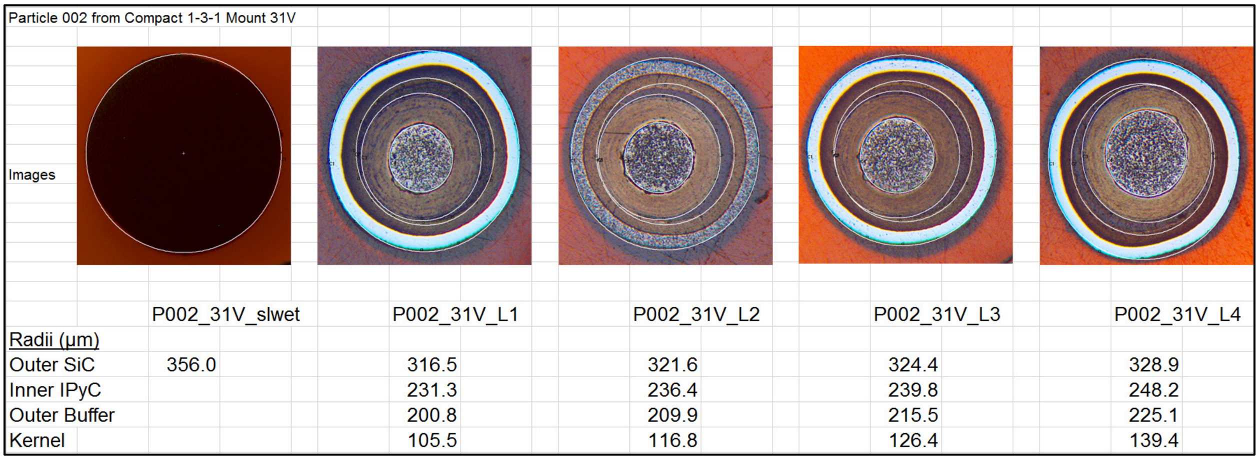

Particle 002 from Compact 1-3-1 Mount 31V

Images

Radii (µm)	P002_31V_slwet	P002_31V_L1	P002_31V_L2	P002_31V_L3	P002_31V_L4
Outer SiC	356.0	316.5	321.6	324.4	328.9
Inner IPyC		231.3	236.4	239.8	248.2
Outer Buffer		200.8	209.9	215.5	225.1
Kernel		105.5	116.8	126.4	139.4

Figure 12. Images and original measurements of AGR-1 particle 002 from Compact 1-3-1, Mount 31V. The white outlines are the circles fitted to 15 user-selected points around the inner or outer boundary of the kernel or layer.

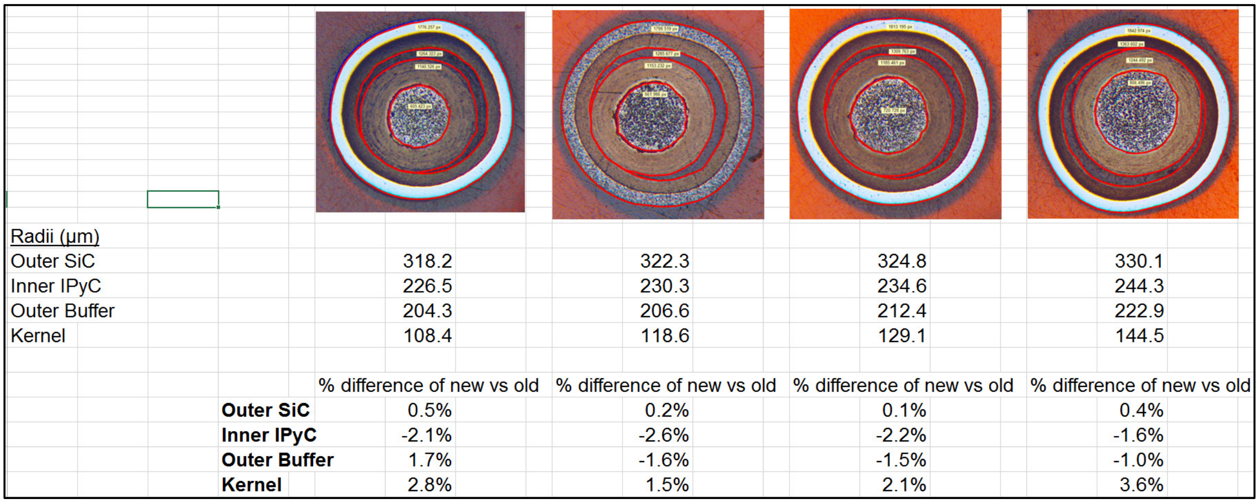

Radii (µm)				
Outer SiC	318.2	322.3	324.8	330.1
Inner IPyC	226.5	230.3	234.6	244.3
Outer Buffer	204.3	206.6	212.4	222.9
Kernel	108.4	118.6	129.1	144.5

	% difference of new vs old	% difference of new vs old	% difference of new vs old	% difference of new vs old
Outer SiC	0.5%	0.2%	0.1%	0.4%
Inner IPyC	-2.1%	-2.6%	-2.2%	-1.6%
Outer Buffer	1.7%	-1.6%	-1.5%	-1.0%
Kernel	2.8%	1.5%	2.1%	3.6%

Figure 13. Images, new measurements, and % difference between the old and new measurements of AGR-1 particle 002 from Compact 1-3-1, Mount 31V.

2.2.6.2 Rejection of certain particles from analysis

Table 3 listed the 10 vials of particles that were mounted for analysis. Approximately 1000 particles were mounted, ground, polished, and imaged. Not all of the particles were suitable for measuring kernel swelling and buffer shrinkage. Some of the particles experienced kernel extrusion through cracks in the buffer layer as shown in Figure 14. Particles exhibiting such features were excluded from quantitative dimensional analysis because the fractured buffers and significant kernel extrusion result in significant departures from sphericity.

A total of 420 AGR-2 particles were determined to be acceptable. Of those, 245 were of the UCO kernel type, and 175 were UO_2. As each particle was analyzed at four cross sections, this resulted in 1680 micrographs on which quantitative measurements were performed (not including the silhouette images). The kernel radius, buffer outer radius, IPyC inner radius, and SiC outer radius were determined based on measurements of their respective circumferences. With these four measurements for each particle at each cross section, a total of 6720 data points were collected and retained. The previous study of AGR-1 Compact 1-3-1 particles analyzed 56 particles (Bower et al. 2017).

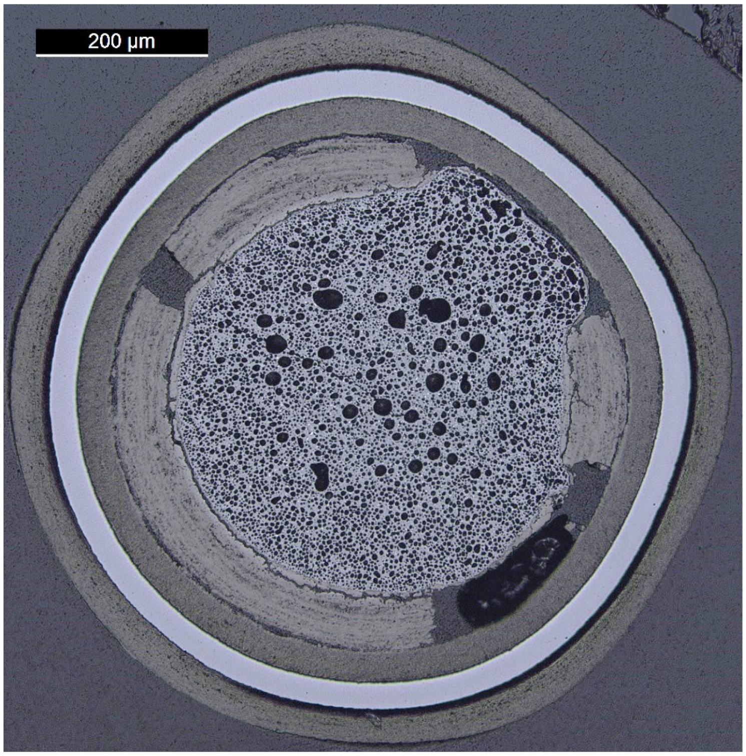

Figure 14. Compact 5-4-2 Particle 1-2, Cross section 3 from Mount 30B, showing extrusion of the kernel through the fractured region of the buffer layer. Particles such as this were excluded from quantitative analysis of the buffer and kernel.

3. CALCULATIONS

The primary data available for calculation of the post-irradiation dimensions are the measured circumferences of the four primary feature boundaries in the TRISO-coated particles: the outer edge of the SiC layer, inner edge of the IPyC, outer edge of the buffer, and the fuel kernel itself. As discussed in Section 2.2, these circumferences were measured in each of four cross sections at varying depths through the particle. In addition, the circumference of one silhouette measurement was obtained for most particles. The silhouette serves as an additional measurement of the outermost circumferences at midplane.

These circumferences were used to estimate the radii of spherical shells, representing the four boundaries, to compare to the equivalent shell radii measured from fuel fabrication. The estimation method is principally that described in (Bower et al. 2017), with minor modifications generally associated with differences in this data set. One of the principal differences in this analysis, compared to the previous study, is that the primary measurements provided for the present mathematical analysis were the circumferences of the shells traced from the micrographs using 100 points per feature boundary, rather than best-fit radii calculated from 16 manually selected points along the feature boundaries.

Major details of the model and uncertainty estimation are described in Sections 3.1 and 3.2. Earlier, Section 2.2.6.1 showed that the calculated radii from four cross sections of the same AGR-1 particle were comparable using either of the two methods; however, a discussion of the differences between the two methods when applied more broadly to different particles is given in Section 3.4.1.[b] Section 3.4.2 discusses how the roughness of the layer interfaces affects both the tracing of the perimeters and the accuracy of the radii and volumes determined from those tracings.

3.1 Mathematical Model

The irradiated particles are idealized as nested spherical shells, and the objective of the analysis is to determine their radii. Towards the outer regions of the particle, the SiC and IPyC layers are concentric. Towards the inner regions of the particle, the buffer and kernel are also concentric with each other, but they are typically are not concentric with the outer layers (as they are in as-fabricated particles) because the inner layers have some freedom when the buffer pulls away from the IPyC.[c]

Consider a model spherical particle (see Figure 15) with a spherical shell radius of r_i. The four spherical shell radii are as follows: r_1 is the SiC outer radius, r_2 is the IPyC inner radius, r_3 is the buffer outer radius, and r_4 is the kernel radius. The total number of shells (m) measured in each particle and used in the analyses is four. In Figure 15, z_M is the vertical offset between the midplane of the two outer shells (i.e., shells with $i = 1$ and $i = 2$) and the midplane of the two inner shells (i.e., shells with $i = 3$ and $i = 4$). The different heights of the different cross sections in the particle are given by z_j. For a total of four cross sections ($k = 4$) through that particle at heights z_1, z_2, z_3, and z_4 above the midplane of the outer shells, one can calculate the circular radii x_{ij} that will be observed in those cross sections using simple geometry. For the two outer layers,

$$x_{ij} = \sqrt{r_i^2 - z_j^2}, \text{ for shells } 1 \leq i \leq 2 \text{ and slices } 1 \leq j \leq k.$$

For the two inner layers,

$$x_{ij} = \sqrt{r_i^2 - (z_j - z_M)^2}, \text{ for shells } 3 \leq i \leq 4 \text{ and } 1 \leq j \leq k, \ |r_i| > |z_j - z_M|.$$

The silhouette measurement of the outermost layer, x_{10}, is expected to be close to r_1. Overall, the situation poses a statistical problem, using $mk+1$ observations to estimate $m+k+1$ parameters. For each of the 420 particles analyzed in this study, $m=4$ and $k=4$, resulting in 17 observations to estimate 9 parameters.

---

[b] The agreement between the fitted spheres may be different than between the measured radii.

[c] Buffer-IPyC separation occurred in all particles observed during AGR-2 compact ceramography (Rice et al. 2018).

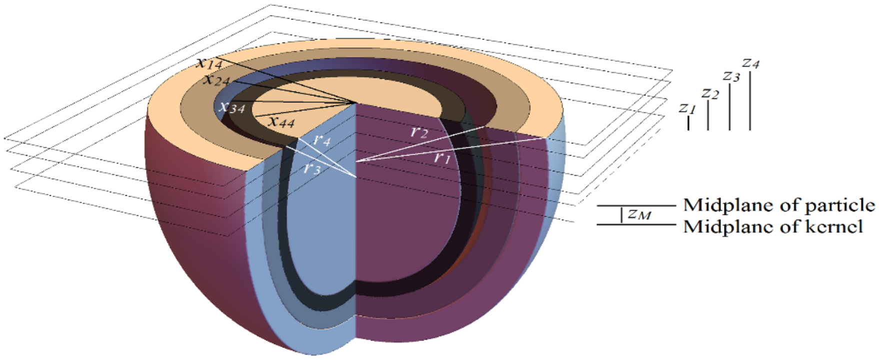

Figure 15. Geometry of an idealized particle. Compare with a typical particle in Figure 17.

When this method is applied to an actual particle, each of the r_i and z_j are fixed, but unknown, and must be calculated from the observations. Meanwhile each of the observations of cross-sectional radii x_{ij} is subject to experimental error. (See Section 3.4 for a discussion of sources of experimental error and uncertainty.) It would be desirable to directly measure the spacing between cross sections, z_1-z_2, z_2-z_3, and z_3-z_4, either through very precise control of the grinding process, or by some other means, such as embedding objects of known dimension into the mount alongside the fuel particles. This would require the estimation of only k+2 parameters and enable more precise determination of the spherical radii for each feature boundary. In practice, conditions on the mount were such that these spacings were known only very approximately (in part because there was variability in local material removal during grinding), and simply using the cross-sectional measurements to calculate both the vertical offsets and the particle radii worked adequately.

3.2 Maximum Likelihood Fitting and Constraints

Maximum likelihood estimation is a widely-used, general-purpose method of fitting a model to a data set. Briefly, given some assumptions about the nature of the random error present in the data, one determines which values of the model parameters (i.e., the radii of the 4 spherical surfaces of interest, the vertical displacement of the kernel and buffer relative to the outer layers, and the altitudes of the 4 cross-sections) would most likely have generated the data that were collected (i.e., the 17 circular radii obtained from the image analysis of the four cross sections). Uncertainty bounds on these parameter values are constructed by observing how much a change in a parameter affects the likelihood of observing the data set.

Given a set of field observations, x_{ij}, on one particle, and a set of candidate values for the parameter estimates, $\hat{r}_i$ and $\hat{z}_j$, the difference between the observed and expected radii can be computed:

$$e_{ij} = x_{ij} - \hat{x}_{ij} = x_{ij} - \sqrt{\hat{r}_i^2 - \hat{z}_j^2}, \text{ for } i=1,2,\ 1 \le j \le 4;$$

$$e_{ij} = x_{ij} - \hat{x}_{ij} = x_{ij} - \sqrt{\hat{r}_i^2 - (\hat{z}_j - \hat{z}_M)^2}, \text{ for } i=3,4,\ 1 \le j \le 4;$$

$$e_{10} = x_{10} - \hat{x}_{10} = x_{10} - \hat{r}_1, \text{ for the silhouette measurement.}$$

Assuming the measurement error for each observation to be approximately normal with mean 0 and standard deviation σ_{ij}, the likelihood function to be maximized is

$$\prod_{\forall i,j} \frac{1}{\sqrt{2\pi}\sigma_{ij}} \exp\left(-\frac{\mathrm{e}_{\mathrm{ij}}^2}{2\sigma_{\mathrm{ij}}^2}\right)$$

Equivalently, taking logarithms and dropping constant terms, one seeks to minimize

$$L = \sum \frac{e_{ij}^2}{\sigma_{ij}^2}$$

In the special case where the σ_{ij} are equal (as they often will be, when all measurements are taken by the same method), this simplifies to minimizing Σe_{ij}^2. The maximum likelihood estimate (MLE) is the set of $\hat{r}_i$ and $\hat{z}_j$ corresponding to the global minimum of L, that is, the usually-unique point at which all of the first partial derivatives of L with respect to each parameter are zero, and all of the second partial derivatives are nonnegative.

A final constraint was applied that required that the shell radii monotonically increase with decreasing shell number (i.e., the layer radii increase from the inside to the outside of the particle). To reduce uncertainty, only particles with complete sets of circumferences (four shells from each of four cross sections) were included in this analysis, which yielded results for 420 particles.

With the exception of particles from Compact 5-4-2, silhouette measurements were obtained on particles after the OPyC layer was removed in an oxidation step (see Section 2.2.2), so that the particle circumference from the silhouette provides a direct constraint on the radius of the SiC shell. For Compact 5-4-2 however, the silhouettes were obtained prior to oxidation of the OPyC shell. Because the OPyC layers are expected to undergo only minor volume change during irradiation, for the purposes of applying a constraint in the calculations, it was assumed – for Compact 5-4-2 – that the effective silhouette radius minus the mean as-fabricated OPyC thickness plus twice its standard deviation, represented a maximum SiC radius for those particles. Compared to predictions made with PARFUME, this is a reasonable assumption. PARFUME predicts that, on average, the OPyC thickness for Capsule 5 particles decreases by 3.5 µm (Hamman 2010). Twice the as-fabricated standard deviation of the OPyC thickness is 5.8 µm, which bounds the predicted change in OPyC thickness.

An implementation of this algorithm was written in MATLAB, and MLEs were obtained for each of the 420 particles that were deemed suitable for detailed analysis. Summary statistics of these are reported in Section 4.

3.3 Calculation of Changes in Radius and Volume

3.3.1 Statistics of ratios of measurements

Relative changes in particle radius or volume are calculated from the ratio of measurements obtained during PIE to those determined prior to irradiation. Because those measurements were not made on the same samples, the mean and variance of the changes must be computed as for the ratio of two independent, normally-distributed, random variables. The approximations used for the mean and variance, obtained from Taylor series expansions for the ratio function (Seltman 2019) for uncorrelated random variables, are as follows.

$$E\left(\frac{X}{Y}\right) \approx \frac{\mu_X}{\mu_X} + \frac{Var(Y)E(X)}{E(Y)^3}$$

$$Var\left(\frac{X}{Y}\right) \approx \frac{Var(X)}{E(Y)^2} + \frac{Var(X)E(X)^2}{E(Y)^4}$$

For these calculations, the distribution parameters for the PIE data were obtained from the distribution of the fitted radii, and did not included the uncertainty of the optimization process.

3.3.2 Calculations of sphere and shell volumes

Sphere and shell volumes were calculated from the radii data as described in (Bower et al. 2017). For a normally distributed random variable, X, with mean μ and variance σ^2, $E[X^3]$ is not just μ^3, but $\mu^3+3\mu\sigma^2$, and $Var[X^3]=9\mu^4\sigma^2+36\sigma^4\mu^2+15\sigma^6$. Thus, given an estimated radius r, the proper estimate of the enclosed volume is $(4/3)\pi(r^3+3r\sigma^2)$. The average volume of an irradiated kernel can either be calculated by finding an estimated volume for each of the particles and averaging them, or by using the mean kernel radius and its standard deviation in the above formula. For the present study, both methods gave the same answer to three significant digits.

This same method can be applied directly to find the total volume of a shell of the particle, as is needed to determine the volume of the buffer, assumed to extend from the outer face of the kernel (r_4) to the outer face of the buffer (r_3) (thereby excluding the “layer” of empty space between the buffer and the IPyC). As above, a bias correction due to not knowing r_3 and r_4 precisely is appropriate in calculating the average buffer volume, as opposed to directly substituting the average inner and outer radii into the equation for buffer volume, $V=(4/3)\pi(r_3^3-r_4^3)$. The unbiased volume estimate is reasonably simple, in terms of r_3, r_4, and their variances s_{r3}^2 and s_{r4}^2: $(4/3)\pi(r_3^3+3r_3s_{r3}^2-r_4^3-3r_4s_{r4}^2)$. However, the variance of this new estimate does not have a convenient closed form. It requires the covariance of r_3^3 and r_4^3, which is not a simple function of the covariance of r_3 and r_4. Therefore average buffer volume was not calculated from the summary statistics. Instead, the quantity $(4/3)\pi(r_3^3-r_4^3)$ was computed for each particle and the mean and standard deviation determined from the distribution of those values.

3.4 Sources of Uncertainty

3.4.1 Tracing interfaces versus best-fit circle

The agreement between the method employed for AGR-1 (circles fit to 16 points) and the method employed for AGR-2 (tracing the perimeter of each layer via 100 points per layer) will vary with the eccentricity of the specific particle and the degree of irregularity of the reconstructed perimeter. Additionally, the 16 points used for circle fitting in AGR-1 and the 100 points per layer used to trace perimeters in AGR-2 were all selected manually and could vary based on the subjectivity of these processes. In Section 2.2.6.1, the AGR-1 particle used for the comparison was reasonably circular, and the two methods agreed within a few percent. Agreement might be less for a less circular particle, or for a highly irregular perimeter trace, and the two methods have different sensitivities to different irregularities.

For a nearly incompressible material, deformation without fracture should preserve volume, but asphericity can lead to some error due to the assumption of sphericity in the calculations. If the cross-sectional volume is preserved in deformation, the radius derived from the perimeter of the trace should accurately reflect the undeformed shell’s cross-sectional radius, but fitting a circle to a section of an ellipse generally yields an underestimate of the radius of the equivalent circle having the same circumference. The ratio of the best-fit circle radius to the radius calculated from its circumference is given as a function of the eccentricity of the ellipse in Figure 16. Eccentricity of the cross-section traces was generally low. As an example, the second cross-section of the kernel of a particle from AGR-2 Compact 6-3-3 (see Figure 17) has an eccentricity typical of the more extreme cases where particles appeared to exhibit asphericity. For the eccentricity of that kernel trace (~0.44), the ratio of the best-fit radius to the radius of the undeformed circle is 0.997. Deformations of that magnitude thus have a practically insignificant effect on the calculation of volume change. To produce even a 5% error in the radius would require an eccentricity of 0.78, where the ratio of the semi-minor to semi-major axis length is 0.9. As no AGR particles with such eccentricity were encountered, both the best-fit circle and circumference-based approach to determining radius should produce little error.

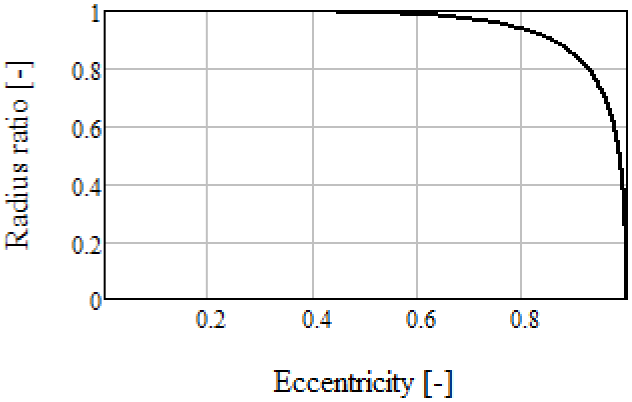

Figure 16. Ratio of best-fit circle radius to the radius calculated from the circumference (perimeter) of an ellipse versus the eccentricity of the ellipse.

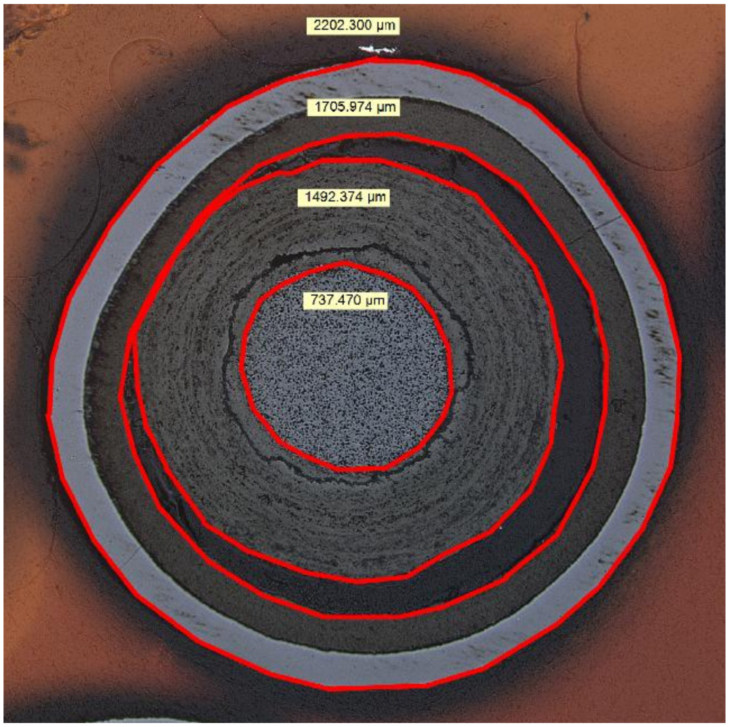

Figure 17. The second cross section of Particle 12-1 in Mount 86A from Compact 6-3-3. Boundary tracings are shown in red. Eccentricity of the kernel trace is 0.44, for which the ratio of lengths of the minor and major axes is 0.9.

3.4.2 Effects of layer interface roughness and irregularities

Irregularities in the trace of a cross-section of a shell can also produce an error in the radius of the implied circle. If the displacement of such features is biased in one direction from the true radius, the effect can be significant, but the induced error is generally minor if the irregularities are unbiased. The radius determined from a best-fit circle (the method used in the prior study), which is essentially the average radius, should be immune to such unbiased variation, but the radius determined from a measured circumference (the approach used in this study) could be significant if the variations are large. In this study, where traces were relatively smooth, and circumference was measured using 100 points to produce each trace, the error should be relatively minor. To illustrate the magnitude of error introduced by variation in the radius of a circle, and how that compares to typical cross-section traces, Figure 18A and Figure 18B show 100-point circular traces around the kernel of the same particle (particle 1-1, from mount 35B, cross section 4, from Compact 5-3-3). Each trace includes an oscillating step in radius, positive and negative, that produces a sawtooth-shaped outline. The 50 periods of the oscillation are evenly distributed along the circumference of the kernel. The magnitude of the periodic deviations in radius in images A and B are, respectively 1.1% and 1.5% of the true radius. In total, trace A would produce a 5% and Trace B a 10% overestimate of the true kernel radius. Figure 18C shows the actual 100 point traces used for the analysis of this particle. The irregularity of the kernel trace in Figure 18C is visibly less than that for the 5% error trace shown in Figure 18A.

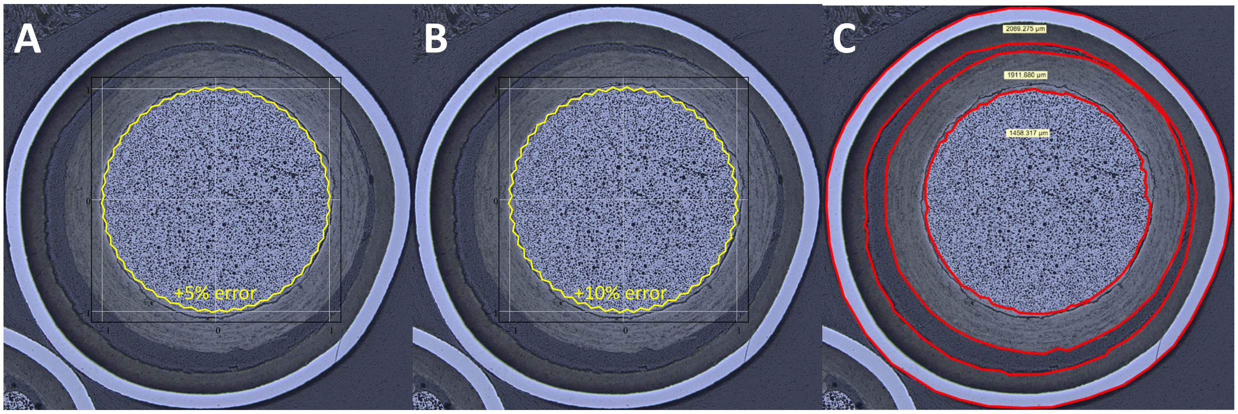

Figure 18. Illustration of periodic irregularities in a circular trace that would produce a +5% error (A) and a +10% error (B) in the radius calculated from measured circumference. Yellow curves reflect 100 points evenly distributed along, and to either side of the true circumference. Red curves denote actual traces used in the analysis of this particle (C).

Different layer morphologies presented challenges for selecting the points that trace the layer circumference. For example, as with AGR-1 (Bower et al. 2017), the buffer layers of some particles had regions of complete buffer-IPyC adhesion, regions of complete buffer-IPyC debonding[d], and regions where narrow strips of the buffer bridged the gap between the bulk of the buffer and the IPyC.[e] An example of this behavior is given in Figure 19 for a particle from AGR-2 Compact 3-3-1. In drawing the perimeter, one must select the points that best represent the true buffer radius. “Small” strips might be reasonably ignored, but larger strips might be accounted for by estimating their thickness and selecting points outside of the buffer outer boundary that would represent this “missing” thickness. In other cases the buffer split so that some portion of it completely detached from the buffer to be adhered to the IPyC (see blue arrows in Figure 19). If the split fragment is small in thickness and length, then it might be reasonably ignored. Larger fragments could be estimated by selecting points along the buffer outer circumference that would trace the circumference if the fragment was still attached to the buffer.

While the AGR-2 Compact 3-3-1 UO_2 kernels have generally well-defined boundaries with the buffer layer (see Figure 19), UCO kernels have an additional feature at the kernel-buffer interface. Figure 20 shows a micrograph of a particle from UCO Compact 6-3-3. A portion of the micrograph has

---

[d] Small, thin pieces of buffer may remain attached to the IPyC while the bulk of the buffer pulls away. In many cases, the pieces are so thin they cannot be measured given the resolution of the images. In those cases, this is reasonably considered to be complete detachment.

[e] Each particle was only observed at 4 planes. The morphology at other, unobserved planes may be different.

been enlarged to show the uranium carbide "skin" that forms at the periphery of the UCO kernels. When UCO fuel kernels were traced at each of four levels to obtain a circumference, the carbide skin was not included.

Error in the estimated radius of a single cross-sectional circle does not generally produce the same degree of error in the fitted shell radius because that radius depends, in this case, on four cross-section radii. Because errors in the calculation of the four sphere shell radii involve fitting of 17 calculated radii, it is difficult to estimate the effect of error in one or more cross-section circles, but the calculation process should minimize the effect of random errors. Uncertainty in the fitted shell radii – induced by errors in the input radii – are incorporated in the uncertainties in the summary measures of particle radii, volume and volume change.

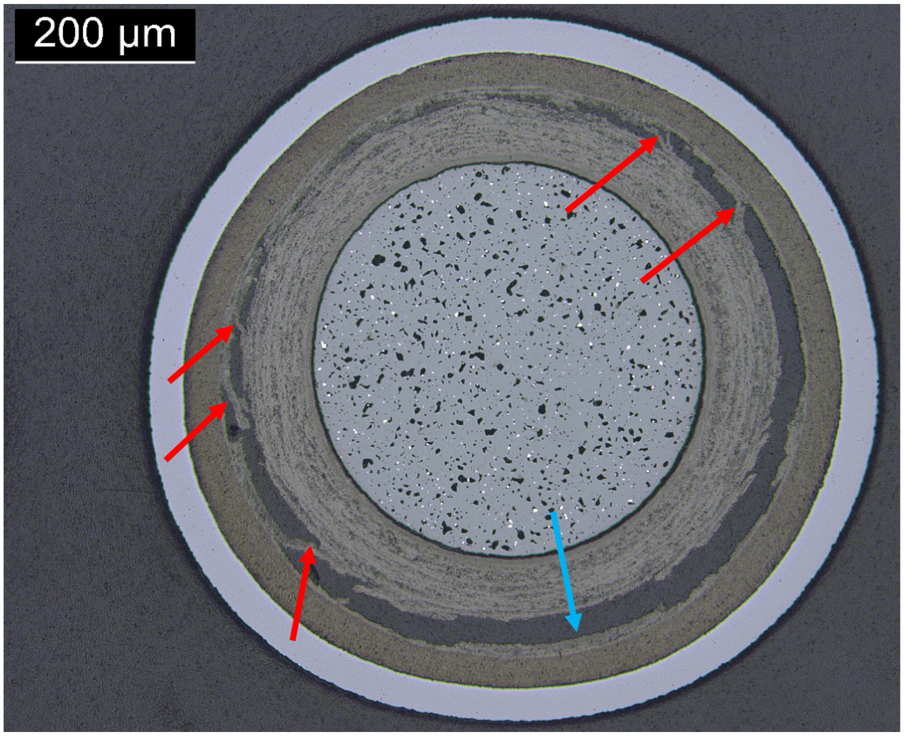

Figure 19. Mount 82A, Cross section 4, Particle 12-4 from UO_2 Compact 3-3-1 (particle ID: MNT82A-CS4-12-4). Red arrows show strips of buffer bridging the IPyC-buffer gap. Blue arrow shows significant buffer fragment adhered to IPyC.

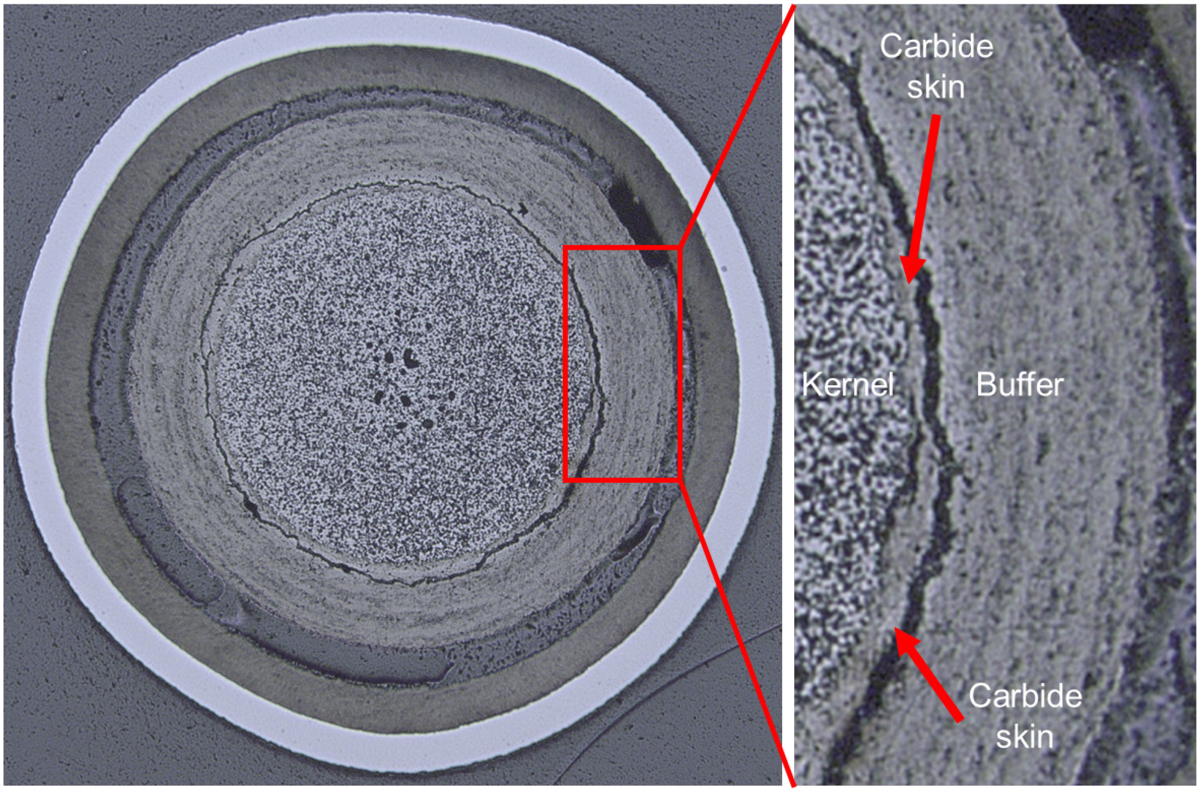

Figure 20. Optical micrograph of Mount 86A, Cross section 4, Particle 5-5 (from UCO Compact 6-3-3). Enlarged region shows example of a uranium carbide skin surrounding the kernel.

3.4.3 Effects of subjectivity and repeatability

In the prior study of AGR-1 particles, the same particle was measured multiple times and the results of the fitted circular radii were compared. The measurement errors appeared to be approximately normally distributed with a standard deviation of about 1 µm, i.e., the majority of replicated measurements clustered in a band ±2 µm from the mean radius. Similarly, measurements were repeated on several AGR-2 particles using the method described in Section 2.2.6.1, and the radii standard deviations were about 1.5 µm. This indicates that replicates were generally within ±3 µm of the mean. The measurements are more repeatable when the cross-sections are clean and the layer interfaces are smooth, and less repeatable when the particles are highly aspherical, when the cross-section passes almost tangentially across the top of a layer, or irregular boundaries exist within the particle (see Section 3.4.2).

4. RESULTS

4.1 TRISO Particle Radii

Spherical radii were calculated using the measurements, described in Section 2.2.6, as input to the mathematical model, described in Section 3. Results were obtained for the following radii: kernel, buffer – outer surface, IPyC – inner surface, and SiC – outer surface. Figure 21 through Figure 24show histograms of the radii for UO_2 Compact 3-3-1, and UCO Compacts 6-3-3, 5-4-2, and 5-3-3, respectively. Figure 25 shows histograms and statistical values when the values for all three UCO compacts are combined into a single population.

The post-irradiation and as-fabricated means (labeled as μ) and standard deviations (labeled as SD) are listed on each histogram, and a probability density function is overlaid as a solid line on each plot for the normal distribution defined by the as-fabricated parameters. The as-fabricated values were taken from the compilation of fuel properties provided in Appendix A of the *AGR-2 Irradiation Test Final As-run Report* (Collin 2018a). The layer thicknesses listed in (Collin 2018a) were determined during as-fabricated fuel characterization by analyzing 50 particles chosen at-random from a composite (combination) of multiple UCO particle batches and a composite of multiple UO_2 batches using the same measurement methods employed for AGR-1. In AGR-1, the as-fabricated fuel kernel diameters were measured by both shadowgraphs and via particle cross sections. The kernel diameters determined from particle cross sections were used to represent the as-fabricated kernel diameter in the AGR-1 study of kernel swelling (Bower et al. 2017). AGR-2 fuel kernel as-fabricated diameters were only measured via shadowgraphs; therefore, the as-fabricated kernel diameters used in this study for AGR-2 were only from shadowgraphs.

Student's t-tests and analysis of variance (ANOVA) were performed to compare the as-fabricated radii to the PIE radii. For UO_2 Compact 3-3-1 and UCO Compact 5-4-2, the SiC layer outer radii did not change in a statistically significant way from the as-fabricated means. According to the t-test, the SiC outer radii for Compacts 6-3-3 and 5-3-3 are slightly larger (by up to about 1.8%) than the as-fabricated values. If the measurement repeatability of ±3 μm is taken into account, the difference is about 0.4% to 1%. This is consistent with the observation that high-purity, chemical vapor deposition β-SiC has very low levels of swelling under irradiation at AGR-2 temperatures and fluences (Snead et al. 2007).

The IPyC inner radii increased compared to the as-fabricated IPyC inner radii. This could be due to IPyC densification (Collin and Ploger 2013). Since the IPyC layers were all well-bonded to the SiC layer, densification would be outward, toward the fixed boundary with the SiC layer. Buffer radii were significantly smaller in all cases, and kernel radii were significantly larger than the as-fabricated radii in all instances. The kernel radii determined from PIE were also compared to each other, and ANOVA did not indicate that the kernels in UCO Compacts 6-3-3, 5-4-2, and 5-3-3 were statistically different in size.

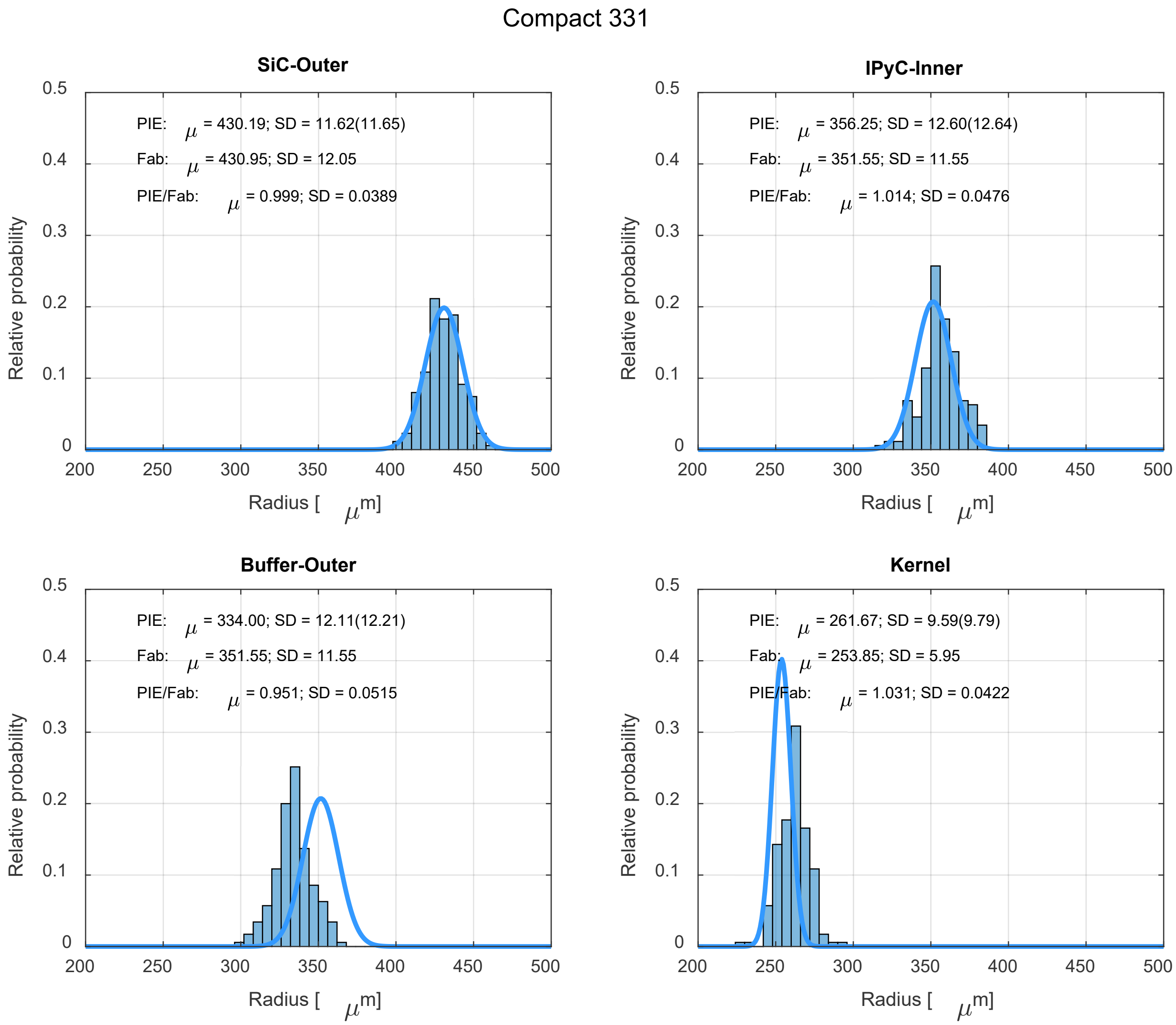

Figure 21. Histograms for radii for particles from AGR-2 UO_2 Compact 3-3-1. PIE distribution parameters (i.e., SD) are for the distribution of fitted means. The SD for the distribution, incorporating the uncertainty of the fit, is given parenthetically.

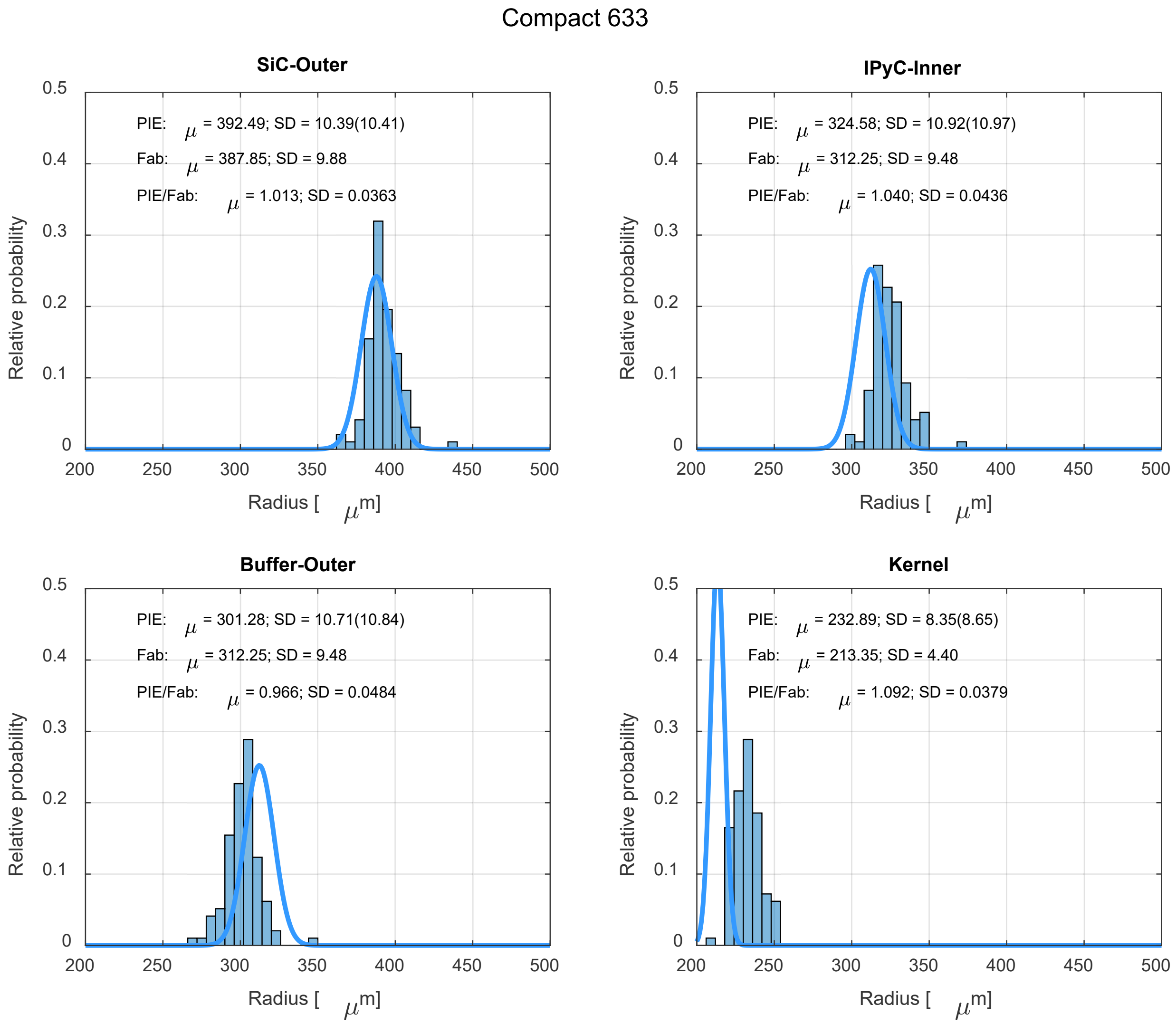

Figure 22. Histograms of radii for particles from AGR-2 UCO Compact 6-3-3. PIE distribution parameters (i.e., SD) are for the distribution of fitted means. The SD for the distribution, incorporating the uncertainty of the fit, is given parenthetically.

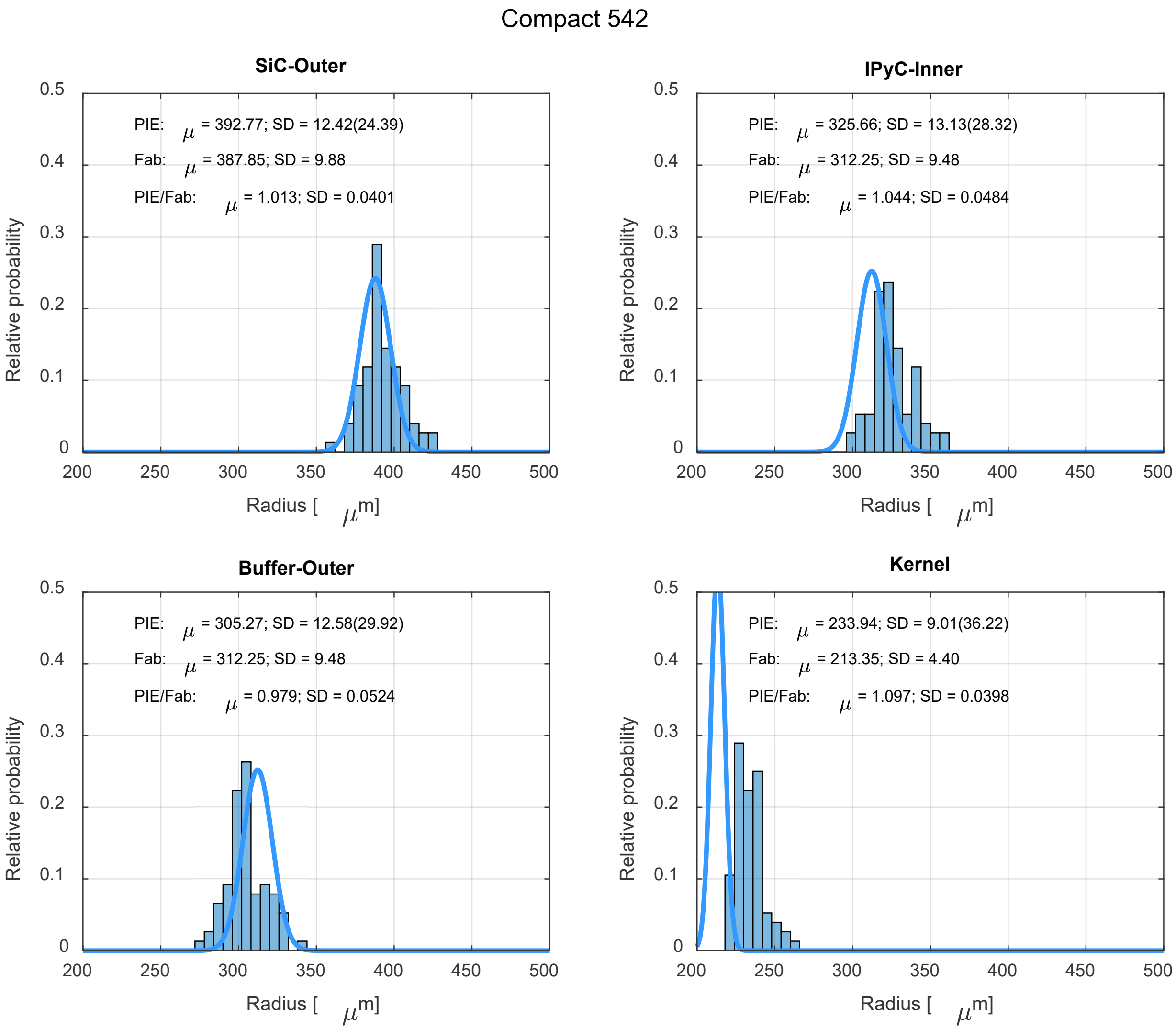

Figure 23. Histograms of radii for particles from AGR-2 UCO Compact 5-4-2. PIE distribution parameters (i.e., SD) are for the distribution of fitted means. The SD for the distribution, incorporating the uncertainty of the fit, is given parenthetically.

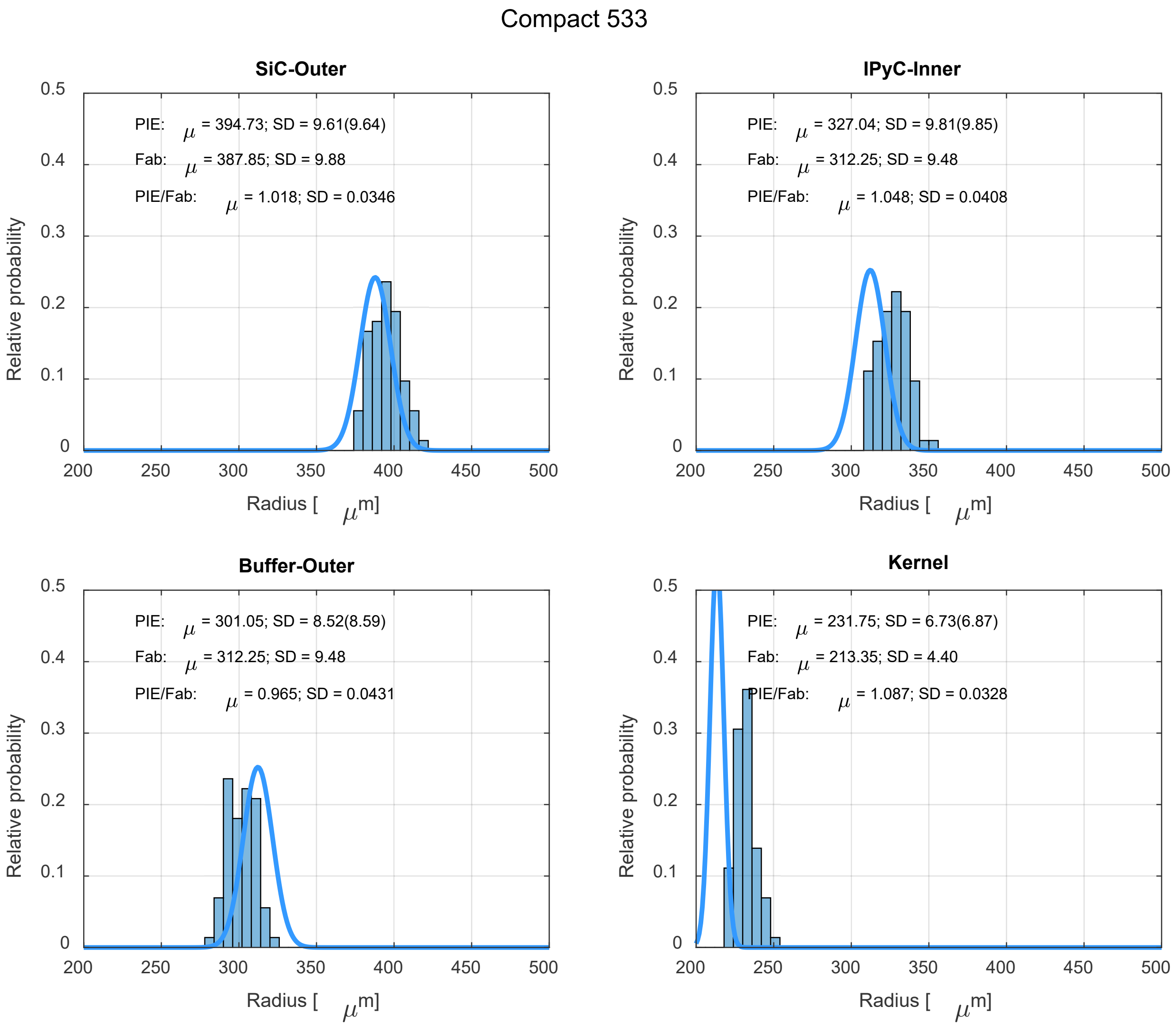

Figure 24. Histograms of radii for particles from AGR-2 UCO Compact 5-3-3. PIE distribution parameters (i.e., SD) are for the distribution of fitted means. The SD for the distribution, incorporating the uncertainty of the fit, is given parenthetically.

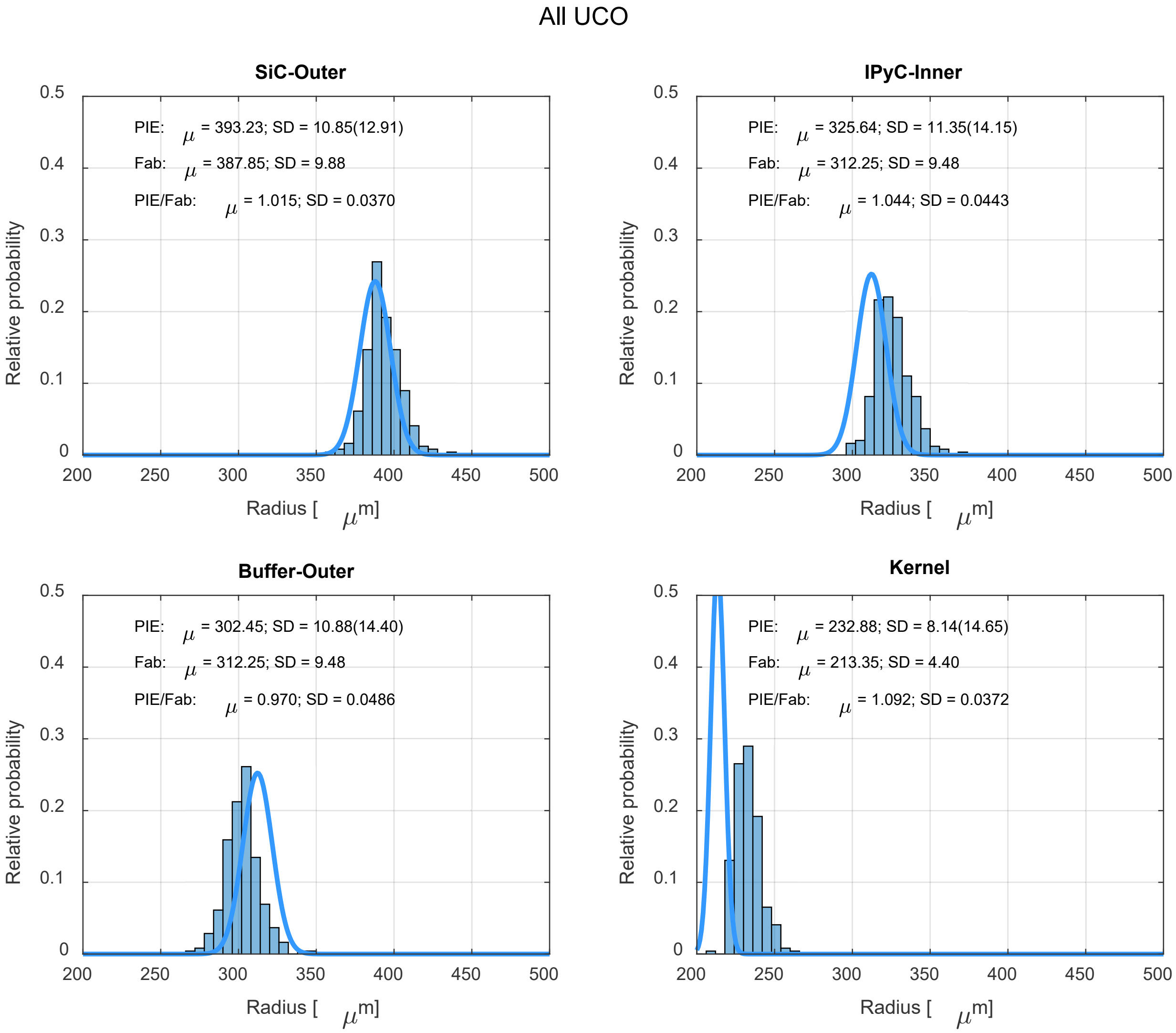

Figure 25. Histograms of radii from combining the data from all AGR-2 UCO compacts analyzed in this study. PIE distribution parameters (i.e., SD) are for the distribution of fitted means. The SD for the distribution, incorporating the uncertainty of the fit, is given parenthetically.

4.2 Kernel Swelling and Buffer Shrinkage

Based on the radii described above, kernel volumetric swelling and buffer volumetric shrinkage has occurred in AGR-2 particles relative to the as-fabricated volumes for the kernels and buffers. The following sections refer to both volume change ratios (i.e., the PIE volume divided by the as-fabricated volume) and the related quantity of volumetric shrinkage and swelling. Percent kernel swelling is defined as follows: (PIE kernel volume/as-fabricated kernel volume – 1)$\times$100. Percent buffer shrinkage is defined as (1 – PIE buffer volume/as-fabricated buffer volume)$\times$100.

Figure 26 shows histograms of kernel and buffer volumes for each of the four AGR-2 compacts analyzed. A probability density function is plotted as a solid line representing the normal distribution of volumes determined from the as-fabricated parameters. A fifth set of histograms (labeled "UCO – All") represents the volume distributions when data from the three AGR-2 UCO compacts are combined into a single population. Kernel volumetric swelling was about 10 ± 10% in UO_2 Compact 3-3-1. The size of the standard deviation in this case indicates that there is some probability that the kernel volume did not change; however, the mean value of 10% swelling is comparable to prior UO_2 studies (see Section 4.4). The UCO kernel swelling ranged from 28 ± 7% for Compact 5-3-3 to 32 ± 9% for Compact 5-4-2.

Unlike kernel swelling, buffer shrinkage was similar for both the UO_2 and UCO fuels. For UCO Compacts 6-3-3, 5-4-2, and 5-3-3, buffer shrinkage was 29 ± 25%, 24 ± 26%, and 28 ± 20%, respectively. UO_2 Compact 3-3-1 had 28 ± 24% buffer shrinkage. The histograms show that the distributions in kernel and buffer volume are slightly broader for the UO_2 compact than for the UCO compacts.

To examine potential influences on kernel and buffer volume changes, fractional changes in kernel and buffer volume, for AGR-2 and AGR-1, were plotted versus irradiation temperature (not shown), burnup, and fast neutron fluence. Figure 27 shows the ratio of the PIE kernel volumes to the as-fabricated volume versus compact burnup. Figure 28 shows the ratio of the PIE buffer volume to the as-fabricated volume versus fast neutron fluence (E>0.18MeV). The plots did not reveal any strong dependence of the measured volumetric changes with those three irradiation parameters.

AGR-1 Compact 1-3-1 kernel swelling and buffer shrinkage were re-calculated here, and the values given in Figure 27 and Figure 28 differ from what was reported in (Bower et al. 2017). In the prior study, the PIE and as-fabricated values were simply divided to give a ratio; however, because the kernels and buffer layers measured in PIE are from a different population of particles than were used in the pre-irradiation fuel characterization measurements, the ratios of the PIE-to-as-fabricated values here are calculated according to Section 3.3.1. The ratios calculated in AGR-1 accounted for the uncertainty in the measured PIE value, but not the uncertainty in the as-fabricated value. The uncertainties for AGR-1 Compact 1-3-1 were also recalculated here to include both the PIE and as-fabricated measurement uncertainties. The new value for AGR-1 Compact 1-3-1 kernel swelling is 27 ± 24% (compared to the original value of 26 ± 6%), and the value for buffer shrinkage is 54% ± 6% (compared to the original value of 39 ± 2%). Note that the small uncertainty in the AGR-1 buffer volume change (compared to the uncertainties in the AGR-2 values) largely reflects the greater difference in the means of the AGR-1 PIE and as-fabricated volumes, which are included in the variance of the ratio.

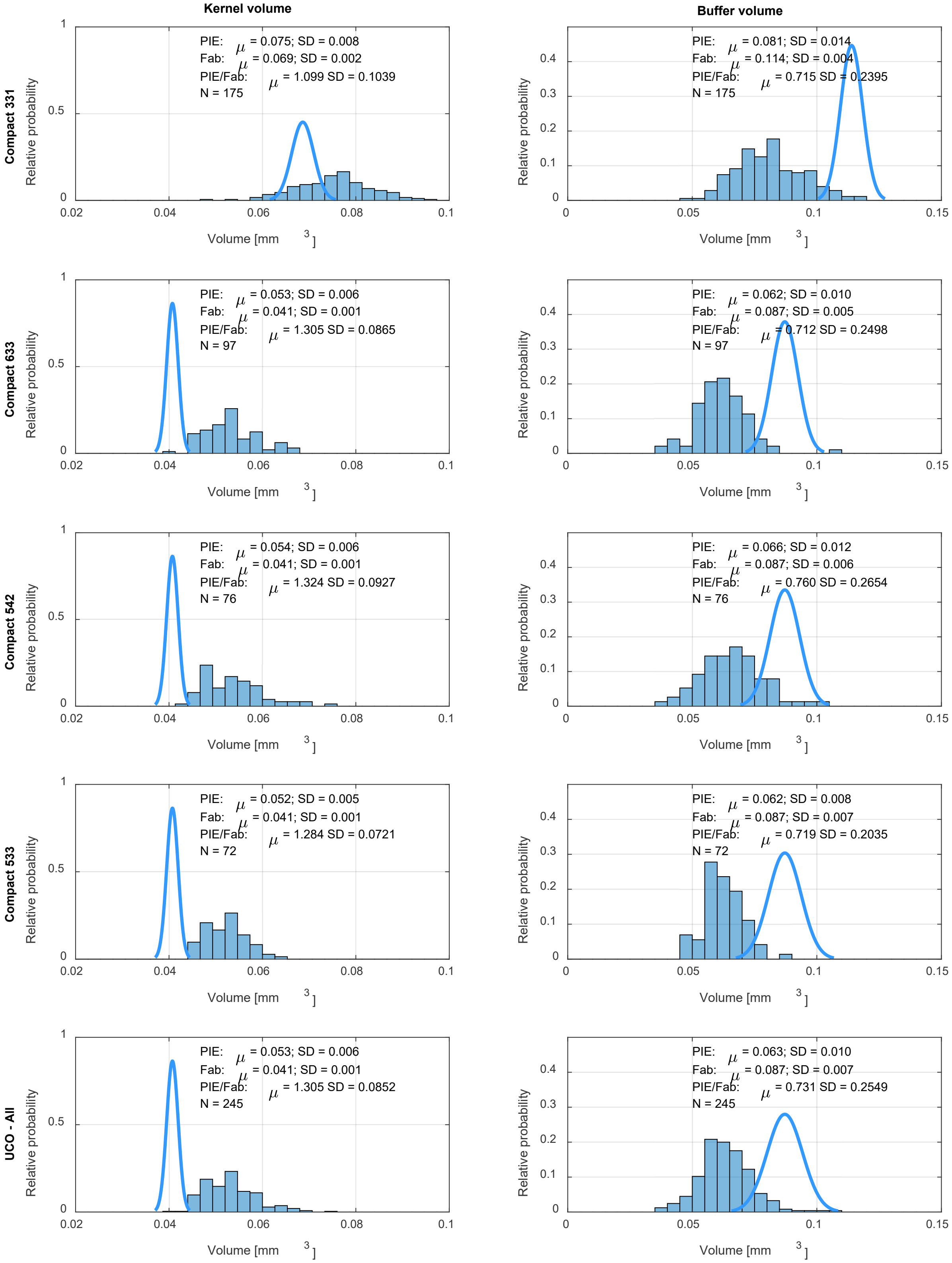

Figure 26. Histograms of kernel and buffer volumetric changes in each AGR-2 compact. The bottom-most histograms combine the values from the three UCO compacts (i.e., 6-3-3, 5-4-2, and 5-3-3) into a single population. PIE distribution parameters are for the distribution of fitted means.

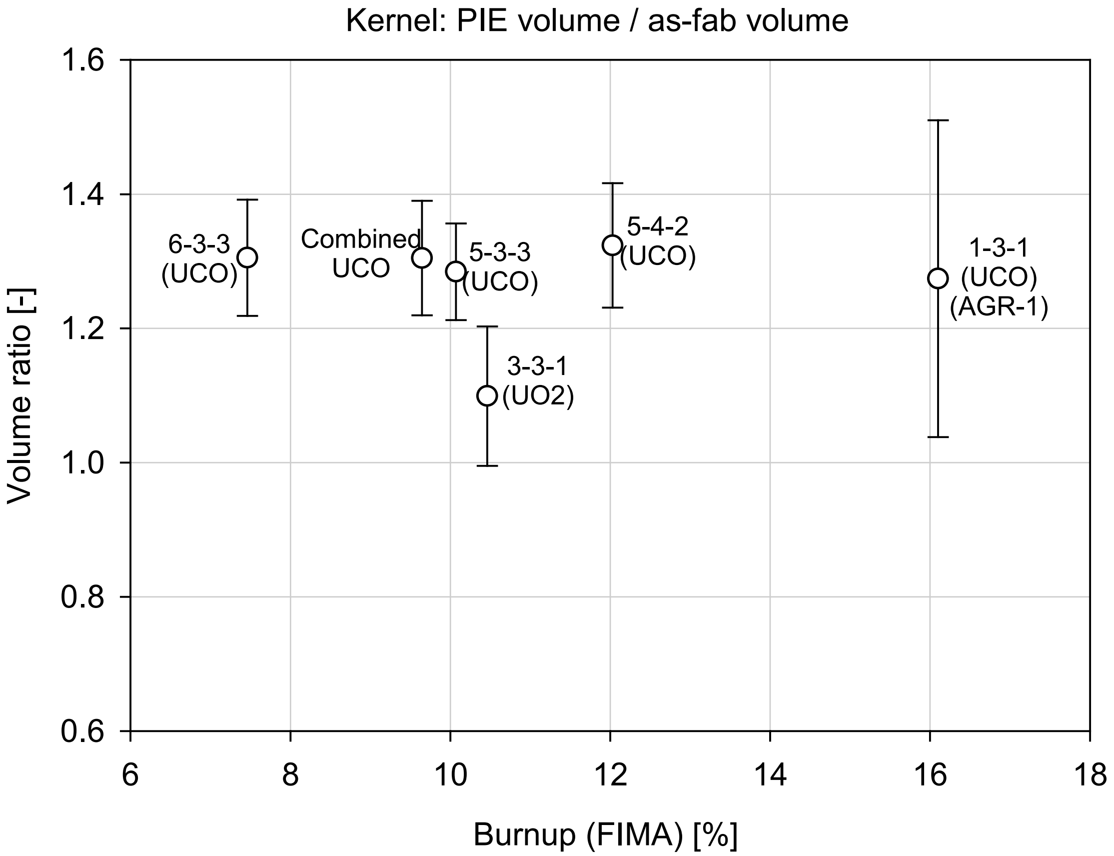

Figure 27. Ratio of PIE kernel volume to as-fabricated volume versus compact burnup. AGR-1 Compact 1-3-1 is also included. Mean and variance of the ratio were calculated as described in Section 3.3.1, with variance of the PIE groups estimated from the distribution of fitted values.

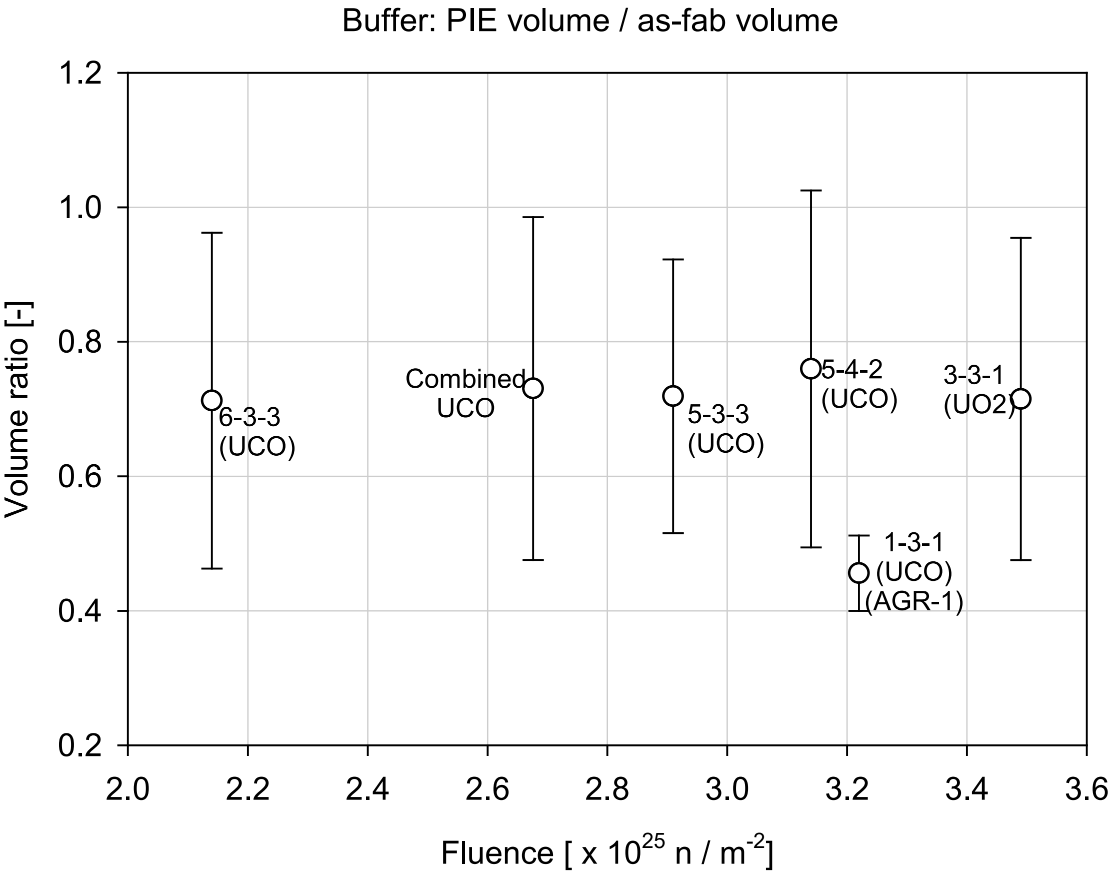

Figure 28. Ratio of PIE buffer volume to as-fabricated volume versus fast neutron fluence (E>0.18MeV). AGR-1 Compact 1-3-1 is also included.

4.3 Post-irradiation Buffer-IPyC gap

As fabricated particles have intact buffer-IPyC bonds; however, irradiation may cause the buffer to detach (fully or partially) from the IPyC. Examples of this behavior can be seen in Figure 17, Figure 19, and Figure 20. The spherical radii determined from PIE for the buffer and IPyC were compared to give average buffer-IPyC gap thicknesses for each of the compacts. Figure 29 plots these gaps as a function of fast neutron fluence, and it is evident that there is little difference between all the AGR-2 compacts. The smallest mean buffer-IPyC gap was 22 ± 6 µm for AGR-2 UO_2 Compact 3-3-1. The largest gap was 26 ± 4 µm for AGR-2 UCO Compact 5-3-3. Similarly, AGR-1 Compact 1-3-1 had a 26 ± 2 µm thick gap (Bower et al. 2017). One of the implications of this gap, is that it may reduce heat transfer within the particle or alter the transport of fission products from the buffer to the IPyC.

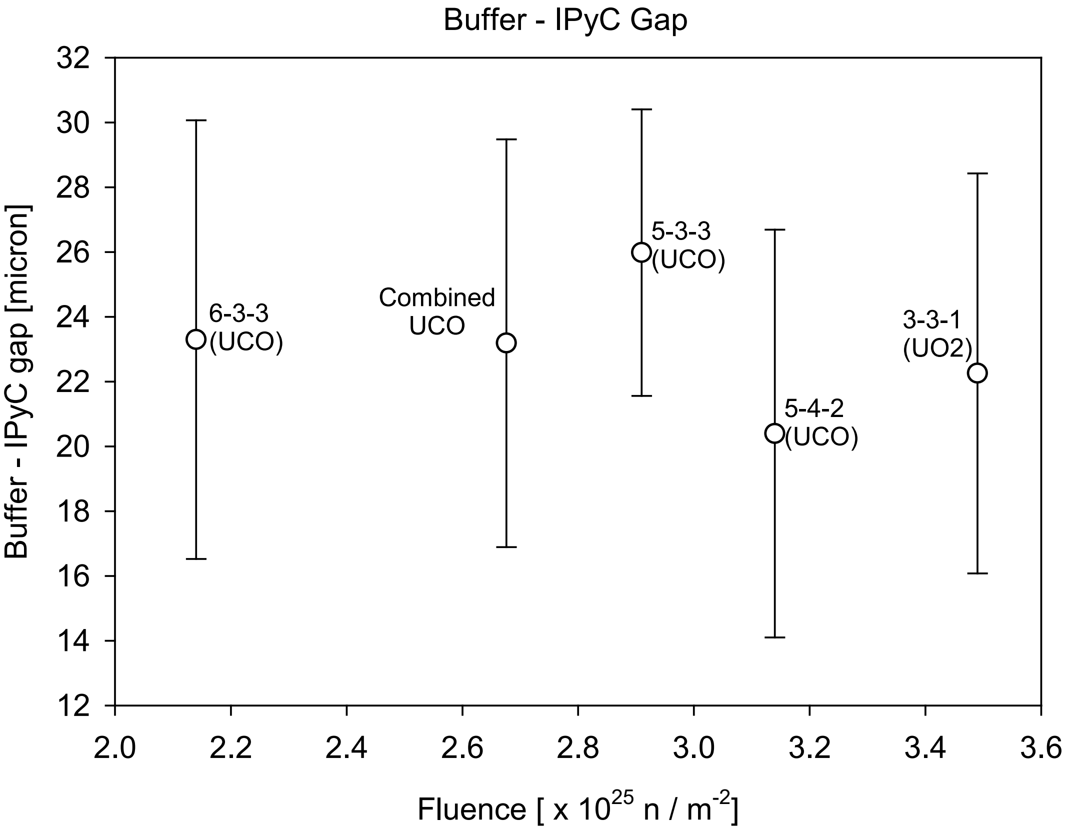

Figure 29. Size of the gap between the buffer and IPyC layers as a function of fast neutron fluence (E>0.18MeV).

4.4 Comparison to prior measurements

Changes of kernel volume in coated particles during irradiation have been reported previously. Results from the current study are compared to previously published data in Figure 30. Proksch et al. (1977) studied dimensional change in UO_2 kernels of varying enrichment (0.7 to 40% U-235) and diameter (220 to 820 µm), covering burnups from 0.5 to 52% FIMA and temperatures from 900 to 1300°C. Dimensional change was determined by x-radiography of particles before and after irradiation. In order to limit the comparison to the most relevant data, only results for 400 µm, 20% enriched bistructural isotropic (BISO) and TRISO particles are presented in Figure 30. The reported irradiation temperature for these particles was 1200°C ±100°C. Volumetric swelling values were derived from the reported percent change in kernel diameter. Proksch et al. noted that overall kernel swelling increased as the kernel diameter decreased.

Bullock and Kaae (1983) and Ketterer et al. (1984) have also reported on particle dimensional change measurements performed as part of the HRB-15A irradiation experiment. Measurements were based on x-radiography of particles before and after irradiation. The individual particles were bonded in graphite trays so that their orientation did not change during irradiation. Results for UO_2, UC_2, and UCO particles (one batch of particles for each fuel type) are included in Figure 30. All of the kernels had an initial diameter of approximately 350 µm and an enrichment of ~19.5%. The UCO kernels had a roughly similar UO_2/UC_2 stoichiometry to the AGR UCO kernels. Burnup values for the irradiated particles were between 26.7 and 29% FIMA and the irradiation temperature for these particle batches was reported to be ~1100–1200°C. Volumetric swelling values were derived from the reported percent change in kernel diameter.

Table 4 lists the data for all results used in the comparison in Figure 30. The volume change data are also expressed as the percent volume change per % FIMA (% change / % FIMA). The AGR-2 UO_2 kernel swelling value (9.9%) appears to be reasonably consistent with the Proksch UO_2 data. The rate of change (0.95% per % FIMA) is at the lower end of the range for the Proksch UO_2 data, but this is consistent with the observation by Proksch et al. that larger kernels tend to have lower swelling rates.[f] The rate of change for the HRB-15A UO_2 particles (1.23% per % FIMA) was also very consistent with the Proksch data in spite of the much higher burnup.

The mean AGR-2 UCO kernel volume change ratios range from 1.28 to 1.32, slightly higher than the mean volume change ratio for AGR-1 of 1.26. Though the uncertainty ranges for AGR-2 and AGR-1 UCO overlap in Figure 30, a t-test at 95% confidence shows that AGR-1 and AGR-2 volume changes are statistically different. While the AGR-2 and AGR-1 volume change ratios are similar, the rate of volume change, however, is significantly higher for AGR-2 than for AGR-1 or the HRB-15A UCO. In the as-fabricated state, AGR-2 UCO kernels were only moderately larger than the HRB-15A UCO or the AGR-1 UCO; thus, it seems unlikely that the differences in initial kernel size can explain the difference in swelling rates between these groups of fuels/experiments. Based on the available data, the reason for the significantly higher swelling rate of the AGR-2 UCO kernels is not known.

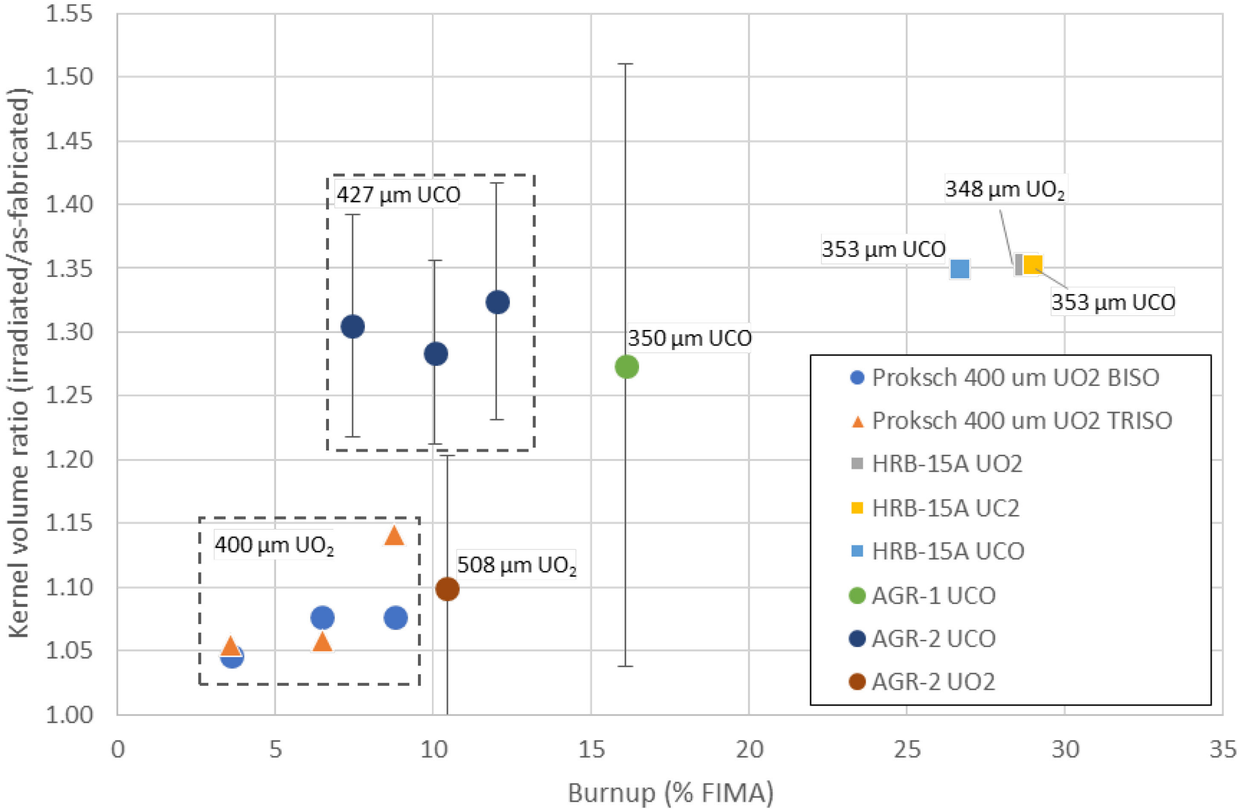

Figure 30. Kernel volume ratio (irradiated/as-fabricated) for UCO, UO_2, and UC_2 coated particles.

---

[f] AGR-2 UO_2 was 508 µm compared to 400 µm for the particles in Proksch et al.

Table 4. As-fabricated fuel kernel data, irradiation conditions, and kernel volume change data for UCO, UO_2, and UC_2 coated particles.

ID	**Fuel type**	**Kernel diameter (μm)**	**Enrichment (% U-235)**	**Burnup (%FIMA)**	**Fast fluence (10^{25} n/m^2, E>0.18MeV)**	**Temperature (°C)**	**Kernel volume ratio**	**% change / % FIMA**
AGR-1 1-3-1	UCO TRISO	350	19.7	16.1	3.22	1092	1.274 ±0.236	1.70
AGR-2 5-3-3	UCO TRISO	427	14	10.1	2.91	1093	1.284 ±0.072	2.82
AGR-2 5-4-2	UCO TRISO	427	14	12.0	3.14	1071	1.324 ±0.093	2.69
AGR-2 6-3-3	UCO TRISO	427	14	7.5	2.14	1060	1.305 ±0.087	4.09
AGR-2 3-3-1	UO_2 TRISO	508	9.6	10.5	3.49	1062	1.099 ±0.104	0.95
HRB-15A	UC_2 TRISO	349	19.5	29	6.4	1100-1200	1.353	1.22
HRB-15A	UO_2 TRISO	348	19.5	28.8	6.4	1100-1200	1.353	1.23
HRB-15A	UCO TRISO	353	19.5	26.7	5.8	1100-1200	1.349	1.31
Proksch	UO_2 BISO	400	20	3.6	NA	1200 ±100	1.046	1.27
Proksch	UO_2 BISO	400	20	6.5	NA	1200 ±100	1.076	1.18
Proksch	UO_2 BISO	400	20	8.8	NA	1200 ±100	1.077	0.88
Proksch	UO_2 TRISO	400	20	3.6	NA	1200 ±100	1.055	1.52
Proksch	UO_2 TRISO	400	20	6.5	NA	1200 ±100	1.058	0.90
Proksch	UO_2 TRISO	400	20	8.8	NA	1200 ±100	1.142	1.61
NA: not available								

5. CONCLUSIONS

A total of 1000 particles from four different AGR-2 fuel compacts (three UCO compacts and one UO_2 compact) were mounted in epoxy and subjected to four rounds of grinding and polishing. After each round, the particle cross sections were imaged, and the kernel and TRISO layers were measured. By backlighting the translucent mounts so that the particles projected a shadow (or silhouette) the particle outer diameters could be determined by automated processes. Measurements were made on the cross sections by manually selecting 100 points around the perimeter of the TRISO particle feature boundaries (ie., kernel, buffer-outer, IPyC-inner, and SiC-outer). Data collected from 420 of the 1000 particles were deemed suitable for calculations of kernel and buffer irradiation-induced volumetric changes.

Among the three AGR-2 UCO compacts, kernel swelling ranged from 28 ± 7% to 32 ± 9%, compared to 27 ± 24% for AGR-1 UCO Compact 1-3-1. This extent of swelling was reached at lower burnups in AGR-2, indicating a faster swelling rate in AGR-2 UCO than in AGR-1 UCO. It is unclear why AGR-2 kernel swelling was more rapid. AGR-2 UO_2 kernel swelling was measured at 10 ± 10%, and the value of this mean was comparable to prior studies of UO_2 swelling in coated particle fuel.

AGR PIE has observed that buffer shrinkage may lead to IPyC cracking, which may allow fission products (e.g., Pd) and uranium to concentrate at, and react chemically with, the SiC layer. Therefore, buffer behavior may impact AGR fuel performance. Buffer shrinkage was similar for both UCO and UO_2 fuels and ranged from 24 ± 26% to 28 ± 20%. This is less than the 54 ± 6% buffer shrinkage observed for AGR-1 Compact 1-3-1. The buffer commonly pulls away from the IPyC without cracking the IPyC or causing any discernable TRISO coating degradation; however, the gap that opens up between the buffer and IPyC may reduce heat transfer within the particle and alter the transport of fission products from the buffer to the IPyC. Average AGR-2 buffer-IPyC gaps in UCO and UO_2 ranged from 22 ± 6 µm to 26 ± 4 µm thick.

In this study, the radii of cross-sections of particle shells were determined via manual selection of 100 points along the perimeter of each layer. This method can better account for cross sections that depart from sphericity than the prior method of picking 16 points and fitting a circle to those points. However, both methods are subject to errors introduced when the surface is very rough or irregular. This is often the case when distinguishing the carbide skin on the outside of the kernel from the bulk of the UCO kernel itself. Another case of an irregular surface is due to partial buffer-IPyC separation, where parts of the buffer may split and remain bonded to the IPyC, or tendrils of the buffer may span the gap between the buffer and IPyC. In either of the two methods, the points are selected manually and subject to the repeatability of the experimenter. In prior studies outside of the AGR program, x-ray radiography has been used in studies of kernel volume changes. The advancement of x-ray computed tomography coupled with automated segmentation may enable direct measurements of kernel and TRISO layer volumes over the entire particle volume. Fuel from the AGR-5/6/7 irradiation (which started in February 2018) could be used for future studies of kernel and buffer volumetric changes, including the effects of very high irradiation temperatures ($T \gtrsim 1400$°C).

6. REFERENCES

Bower, G. R., Ploger, S. A., Demkowicz, P. A., Hunn, J. D., 2017, “Measurement of kernel swelling and buffer densification in irradiated UCO-TRISO particles.” *Journal of Nuclear Materials*, Vol. 486, pp. 339-349.

Bullock, R. E. and Kaae, J. L., 1983, “Performance of Coated UO_2 Particles Gettered with ZrC,” *Journal of Nuclear Materials*, Vol. 115, pp. 69-83.

Collin, B. P., and Ploger, S. A., 2013, *AGR-1 PIE Measurements of Kernel Swelling and Buffer Densification, and Comparison to Model Predictions by PARFUME*, ECAR-2206, Idaho National Laboratory, May 2013.

Collin, B. P., 2015a, *AGR-1 Irradiation Test Final As-Run Report*, INL/EXT-10-18097, Rev. 3, Idaho National Laboratory, January 2015.

Collin, B. P., 2015b, *AGR-3/4 Irradiation Test Final As-Run Report*, INL/EXT-15-35550, Rev. 0, Idaho National Laboratory, June 2015.

Collin, B. P., 2018a, *AGR-2 Irradiation Test Final As-Run Report*, INL/EXT-14-32277, Rev. 4, Idaho National Laboratory, February 2018.

Collin, B. P., 2018b, *AGR-5/6/7 Irradiation Experiment Test Plan*, PLN-5245, Rev. 1, Idaho National Laboratory, January 2018.

Demkowicz, P. A., 2013, *AGR-2 Post-Irradiation Examination Plan*, PLN-4616, Rev. 0, Idaho National Laboratory, December 2013.

Demkowicz, P. A., Hunn, J. D., Morris, R. N., van Rooyen, I., Gerczak, T., Harp, J. M. and S.A. Ploger, 2015, "AGR-1 Post-Irradiation Examination Final Report," INL/EXT-15-36407, Idaho National Laboratory, August 2015.

Demkowicz, P. A., Hunn, J. D., Ploger, S. A., Morris, R. N., Baldwin, C. A., Harp, J. M., Winston, P. L., Gerczak, T. J., van Rooyen, I. J., Montgomery, F. C., and Silva, C. M., 2016, "Irradiation performance of AGR-1 high temperature reactor fuel," *Nuclear Engineering and Design*, Vol. 306, pp. 2-13.

Demkowicz, P. A., 2017, *AGR-3/4 Phase 2 Post-Irradiation Examination Plan*, PLN-5382, Idaho National Laboratory, May 2017.

Gerczak, T. J., Hunn, J. D., Morris, R. N., Montgomery, F. C., Skitt, D. J., Baldwin, C. A., Dyer, J. A., Eckhart, B. D., 2018, "Analysis of fission product distribution and composition in the TRISO layers of AGR-2 fuel," *Proceedings of HTR-2018*, *Warsaw, Poland, October 8–10, 2018*, Paper HTR2018-0048.

Hamman, K. D., *AGR-2 Pre-Test Prediction Analyses using the PARFUME Code for U.S. Fuel Particles*, ECAR-1020, Rev. 0, Idaho National Laboratory, June 2010.

Hawkes, G., 2014a, *AGR-1 Daily As-Run Thermal Analyses*, ECAR-9638, Rev. 4, Idaho National Laboratory, September 2014.

Hawkes, G., 2014b, *AGR-2 Daily As-Run Thermal Analyses*, ECAR-2476, Rev. 1, Idaho National Laboratory, August 2014.

Hunn, J.D., Savage, T.W., and Chinthaka Silva, 2010, *AGR-2 Fuel Compact Pre-Irradiation Characterization Summary Report*, ORNL/TM-2010/226, Oak Ridge National Laboratory, November 2010.

Hunn, J. D., Baldwin, C. A., Gerczak, T. J., Montgomery, F. C., Morris, R. N., Silva, C. M., Demkowicz, P. A., Harp, J. M., Ploger, S. A., 2016, "Detection and analysis of particles with failed SiC in AGR-1 fuel compacts", *Nuclear Engineering and Design*, Vol. 306, pp. 34-46.

Hunn, J.D., Morris, R.N., Montgomery, F.C., Gerczak, T. J., Skitt, D. J., Baldwin, C. A., Dyer, J. A., Helmreich, G. W., Eckhart, B. D., Burns, Z. M. Burns, Demkowicz, P. A., and Stempien, J., 2018, "Post-irradiation Examination and Safety Testing of US AGR-2 Irradiation Test Compacts," *Proceedings of HTR-2018, Warsaw, Poland, October 8–10, 2018*.

Idaho National Laboratory, 2018, *Technical Program Plan for INL Advanced Reactor Technologies Advanced Gas Reactor Fuel Development and Qualification Program*, PLN-3636, Rev. 7, June 2018.

Ketterer, J. W., Kania, M. J., Bullock, R. E., and Siman-Tov, I. I., 1984, *Capsule HRB-15A Postirradiation Examination Report*, GA-A16758, GA Technologies, July 1984.

Miller, G. K., Petti, D. A., Maki, J. T., Knudsen, D. L., and Skerjanc, W.F., 2018, *PARFUME Theory and Model Basis Report*, INL/EXT-08-14497, Idaho National Laboratory, September 2018.

Proksch, E., Knotik, K., and Strigl, A., 1977, "Abbrandbedingtes Schwellen Hochdichter Oxidischer HTR-Brennstoffkerne," *Journal of Nuclear Materials*, Vol. 66, pp. 263-272.

Rice, F. J., Stempien, J. D., and Demkowicz, P. A., 2018, "Ceramography of irradiated TRISO fuel from the AGR-2 experiment," *Nuclear Engineering and Design*, Vol. 329, pp. 73-81.

Seltman, H., *Approximations for Mean and Variance of a Ratio*, http://www.stat.cmu.edu/~hseltman/files/ratio.pdf, Web page visited June 8, 2019.

Snead, L. L., Nozawa, T., Katoh, Y., Byun, T., Kondo, S., and Petti, D. A., 2007, "Handbook of SiC properties for fuel performance modeling," *Journal of Nuclear Materials*, Vol. 371, pp. 329-377.

Sterbentz, J. W., 2013, *JMOCUP As-Run Daily Depletion Calculation for the AGR-1 Experiment in ATR B-10 Position*, ECAR-958, Rev. 2, September 2013, Idaho National Laboratory.

Sterbentz, J. W., 2014, *JMOCUP As-Run Daily Depletion Calculation for the AGR-2 Experiment in ATR B-12 Position*, ECAR-2066, Rev. 2, April 2014, Idaho National Laboratory.

van Rooyen, I. J., Janney, D. E., Miller, B. D., Demkowicz, P. A., and Riesterer, J., 2014, "Electron microscopic evaluation and fission product identification of irradiated TRISO coated particles from the AGR-1 experiment: A preliminary review," *Nuclear Engineering and Design*, Vol. 271, pp. 114-122.